



Water Resources Research

RESEARCH ARTICLE

10.1002/2015WR017637

Special Section:

The 50th Anniversary of Water Resources Research

Key Points:

- Subsurface agricultural drainage alters hydrologic response
- Climate filtered through engineered landscapes linearizes streamflow dynamics
- Amplified hydrology modulates ecological transitions

Correspondence to:

E. Foufoula-Georgiou,
efi@umn.edu

Citation:

Foufoula-Georgiou, E., Z. Takbiri, J. A. Czuba, and J. Schwenk (2015), The change of nature and the nature of change in agricultural landscapes: Hydrologic regime shifts modulate ecological transitions, *Water Resour. Res.*, 51, 6649–6671, doi:10.1002/2015WR017637.

Received 29 MAY 2015

Accepted 10 JUL 2015

Accepted article online 14 JUL 2015

Published online 27 AUG 2015

The change of nature and the nature of change in agricultural landscapes: Hydrologic regime shifts modulate ecological transitions

Efi Foufoula-Georgiou¹, Zeinab Takbiri¹, Jonathan A. Czuba¹, and Jon Schwenk¹

¹Department of Civil, Environmental, and Geo-Engineering, St. Anthony Falls Laboratory and National Center for Earth-Surface Dynamics, University of Minnesota, Minneapolis, Minnesota, USA

Abstract Hydrology in many agricultural landscapes around the world is changing in unprecedented ways due to the development of extensive surface and subsurface drainage systems that optimize productivity. This plumbing of the landscape alters water pathways, timings, and storage, creating new regimes of hydrologic response and driving a chain of environmental changes in sediment dynamics, nutrient cycling, and river ecology. In this work, we nonparametrically quantify the nature of hydrologic change in the Minnesota River Basin, an intensively managed agricultural landscape, and study how this change might modulate ecological transitions. During the growing season when climate effects are shown to be minimal, daily streamflow hydrographs exhibit sharper rising limbs and stronger dependence on the previous-day precipitation. We also find a changed storage-discharge relationship and show that the artificial landscape connectivity has most drastically affected the rainfall-runoff relationship at intermediate quantiles. Considering the whole year, we show that the combined climate and land use change effects reduce the inherent nonlinearity in the dynamics of daily streamflow, perhaps reflecting a more linearized engineered hydrologic system. Using a simplified dynamic interaction model that couples hydrology to river ecology, we demonstrate how the observed hydrologic change and/or the discharge-driven sediment generation dynamics may have modulated a regime shift in river ecology, namely extirpation of native mussel populations. We posit that such nonparametric analyses and reduced complexity modeling can provide more insight than highly parameterized models and can guide development of vulnerability assessments and integrated watershed management frameworks.

1. Introduction

In a recent study, *Joiner et al.* [2014] reported that the “brightest” spot on Earth in terms of fluorescent glow, an indicator of photosynthetic activity and gross productivity, is the midwestern region of the United States during the growing season. In fact, the “corn belt” was found to be 40% more biologically productive during July than the lush Amazonian rainforest. This is the result of the intensification and expansion of agriculture due to the ever-growing demand for corn and soybeans that are supplanting small grains, and the human ingenuity that keeps plants as healthy and productive as possible by controlling their water intake. Managing plant water availability to keep plant roots dry during the growing season requires artificial drainage systems created by installing millions of miles of subsurface drainage tiles per year. Unsurprisingly, this subsurface plumbing of hydrologic pathways changes the magnitude (increased volume of streamflow hydrographs), time response (faster delivery to streams), and partitioning of surface and subsurface contributions to streamflow in these watersheds (see the extensive review of *Blann et al.* [2009, and references therein]).

Figure 1 illustrates this hydrologic regime shift by showing the daily precipitation and streamflow series of the Redwood basin, a subbasin of the Minnesota River Basin (MRB), during 2 years: 1971, when small grains and soybeans accounted each for approximately 15% of the basin area, and 2002, when small grains covered 3% while soybean cover increased to almost 40% of the basin. Although total annual precipitation was similar during these 2 years (total depths of 610 and 640 mm, respectively), streamflow increased by almost a factor of three (mean annual flows of $2.3 \text{ m}^3/\text{s}$ in 1971 and $6.0 \text{ m}^3/\text{s}$ in 2002). A closer look at the daily streamflow series during these 2 years reveals a complex hydrologic change including higher peaks, faster

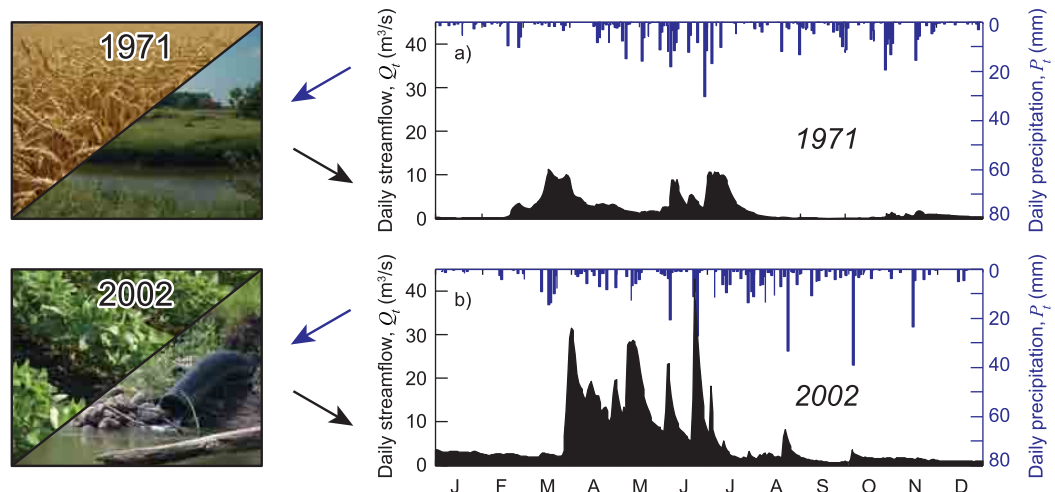


Figure 1. An illustration of hydrologic change in a midwestern agricultural basin. Observed daily precipitation and streamflow series for the Redwood basin in (a) 1971 (when hay and small grains were more widespread) and (b) 2002 (when soybeans and agricultural drainage became more prevalent). Total annual precipitation was 610 and 640 mm in 1971 and 2002, respectively, while mean annual streamflow was 2.3 and 6.0 m^3/s .

rising limbs of hydrographs, altered falling limbs, and increased base flow spanning several time scales. To gain insight into the hydrologic changes due mainly to intensified agriculture (land-cover change and artificial drainage), we performed a detailed analysis of the hydrologic response during the growing season of May and June, when climate-related precipitation changes were minimal. We also analyzed the yearlong streamflow dynamics to quantify the combined climate/land use effects.

Hydrologic changes in a watershed trigger a cascade of often undesirable geomorphic and ecologic changes [e.g., Konar *et al.*, 2013], and the MRB, in particular, is geologically predisposed to amplify the effects of hydrologic change due to increased sediment production (e.g., see Belmont *et al.* [2011] and discussion in section 2). Within the basin, 336 river reaches are currently listed as impaired under the Clean Water Act for excessive sediment and nutrients as well as degraded aquatic life [Carlisle *et al.*, 2011]. This has prompted the state of Minnesota to pass an amendment to the Minnesota constitution (the Clean Water, Land, and Legacy Amendment) that increases the state sales tax during 2009–2034 with a portion of this revenue devoted to protecting, enhancing, and restoring water quality in lakes, rivers, and streams [Legislative Coordinating Commission, 2014]. Mitigation planning efforts require a thorough understanding of changes and integrated watershed-scale models of hydrologic and environmental response to evaluate alternative scenarios of change.

Physically based hydrologic models that incorporate changes in land use and agricultural practices require extensive data for calibration (see De Schepper *et al.* [2015] for a nice review of available models) and insight may be obscured due to the many parameters, complicated physics, and large computational resources required to perform simulations of large watersheds. Yet understanding and quantifying the nature of these hydrologic changes and how they cascade to other environmental and ecological changes, such as sediment production, storage, and transport, changes in river morphology, nutrient cycling, and alteration of the number and diversity of native riverine species are important for river basin mitigation and planning.

In this paper, we seek to understand the nature of hydrologic change in the intensively managed agricultural MRB and quantify how a hydrologic shift might cascade to river ecosystems. We begin by providing geologic, climatic, and land use context of the MRB in section 2 and establish the connection between agricultural land use change and hydrologic change. In section 3, we analyze the hydrologic response during the growing season via Copula analysis to detect changes in the magnitude-frequency dependence of the rising (and falling) hydrograph limbs on the previous-day rain (and streamflow). We also perform time-frequency and phase-space analyses of the yearlong daily streamflows and precipitation, when both climate and land use changes are at play, to detect possible changes in their nonlinear dynamics. In section 4, we apply a hydrology-driven, process-based dynamic interaction model that predicts native mussel population abundance [Hansen *et al.*, 2015] to show how altered streamflows and/or sediment production can cause

ecological regime transitions. In section 5, we provide concluding remarks and present some perspectives on a framework for sustainability analysis via reduced complexity modeling and key system vulnerabilities.

2. The Minnesota River Basin: A Landscape Sensitive to Hydrologic Change

2.1. Geologic History and Climate

The Minnesota River Basin drains approximately 44,000 km² of southern Minnesota and parts of South Dakota, Iowa, and North Dakota into the Mississippi River (see inset in Figure 2c). Its geology was set around 14,000 years ago when the last glacial advance of the Des Moines Lobe created a flat landscape dotted with lakes. The catastrophic drainage of Glacial Lake Agassiz around 13,400 years ago created an outburst flood which incised into the proto-Minnesota River and carved the present-day Minnesota River Valley [Ojakangas and Matsch, 1982] leaving behind tributaries hanging above the main stem Minnesota River and initiating multiple knickpoints. Today, these knickpoints have migrated about 40 km upstream and have created knickzones of rapidly incising channels disconnected from their floodplains [Gran et al., 2011, 2013; Belmont, 2011]. As a consequence, steep bluffs, some 60 m high and close to streams, have been created within these knickzones, making the basin prone to accelerated erosion in response to increased precipitation and streamflows [Schottler et al., 2014].

In terms of climate, two major trends have been observed in the MRB: (1) higher temperatures leading to earlier snowmelt and a longer growing season and (2) an increase in precipitation with an intensification of extreme storms [e.g., Lettenmaier et al., 1994; Changnon and Kunkel, 1995; Karl et al., 1996; Angel and Huff, 1997; Michaels et al., 2004; Groisman et al., 2004, 2012; Pryor et al., 2009; Villarini et al., 2011; Higgins and Kousky, 2013; Walsh et al., 2014]. Changes in evaporative and radiative cooling have also been reported and attributed to the enhanced seasonal precipitation signal [e.g., Milly and Dunne, 2001]. Increasing streamflow trends between the early 1900s and early 2000s have been documented in several studies [Lettenmaier et al., 1994; Lins and Slack, 1999; Douglas et al., 2000; Schilling and Libra, 2003; Schilling et al., 2010; Hirsch and Ryberg, 2012], although the attribution of these changes to mainly climate or land use remains controversial (e.g., see Frans et al. [2013] for discussion and references on both sides). Within the MRB, significant streamflow change has been documented over the past three decades with increased mean daily flow, 7 day low flow, and peak daily flow [e.g., Novotny and Stefan, 2007; Dadaser-Celik and Stefan, 2009].

2.2. Human Modifications

The MRB has a long history of direct human influences on its landscape through large-scale agriculture. Historically, around the time of European settlement in the mid-1800s, the MRB was dominated by tall-grass prairie and dotted with poorly drained wetlands [Marschner, 1974]. Beginning in the late 1800s, these wetlands were drained for agriculture with the construction of surface ditches and installation of subsurface drain tiles [Moline, 1969; Dahl and Allord, 1996]. While agriculture has largely dominated the MRB since the early 1900s, at that time it mostly included hay and small grains (barley, flax, oats, rye, and wheat). Over time these crops were replaced by soybeans while the number of acres of land for growing corn only slightly increased (e.g., see Figure 2) [U.S. Department of Agriculture (USDA), 2014]. The crop conversion to soybeans is hydrologically significant because it often involves the installation of extensive subsurface drain tiles and affects seasonal evapotranspiration potential [e.g., Zhang and Schilling, 2006; Schottler et al., 2014].

Crop conversion to soybeans has taken place progressively within the MRB. To quantify this progression, we define here the “Land-Cover Transition” (LCT) as the year when the percentage of soybean cover exceeded that of hay and small grains. This year was computed from 5 year running averages of county-level land-cover data available from USDA [2014] (Figure 2). We observe that the LCT progressively shifted from the late 1950s and early 1960s in the southeastern MRB to the 1990s and 2000s in the northwestern MRB.

In addition to the LCT, we define the “Hydrologic Transition” (HT) as the year marking a transition to amplified daily streamflows triggered by the expansion and intensification of agricultural drainage. Unfortunately, data on the extent and intensity of subsurface drain tiles are mostly unavailable. However, the 1970s were a pivotal time for agricultural drainage in the MRB when plastic drain tiles, which were cheaper and easier to install, became more widespread and replaced old clay tiles [Stuyt et al., 2005]. Several studies have also shown that this period corresponded to observed major hydrologic changes in the region [e.g., Schilling and Libra, 2003; Raymond et al., 2008; Schottler et al., 2014]. The 1970s, then, represent the earliest period in

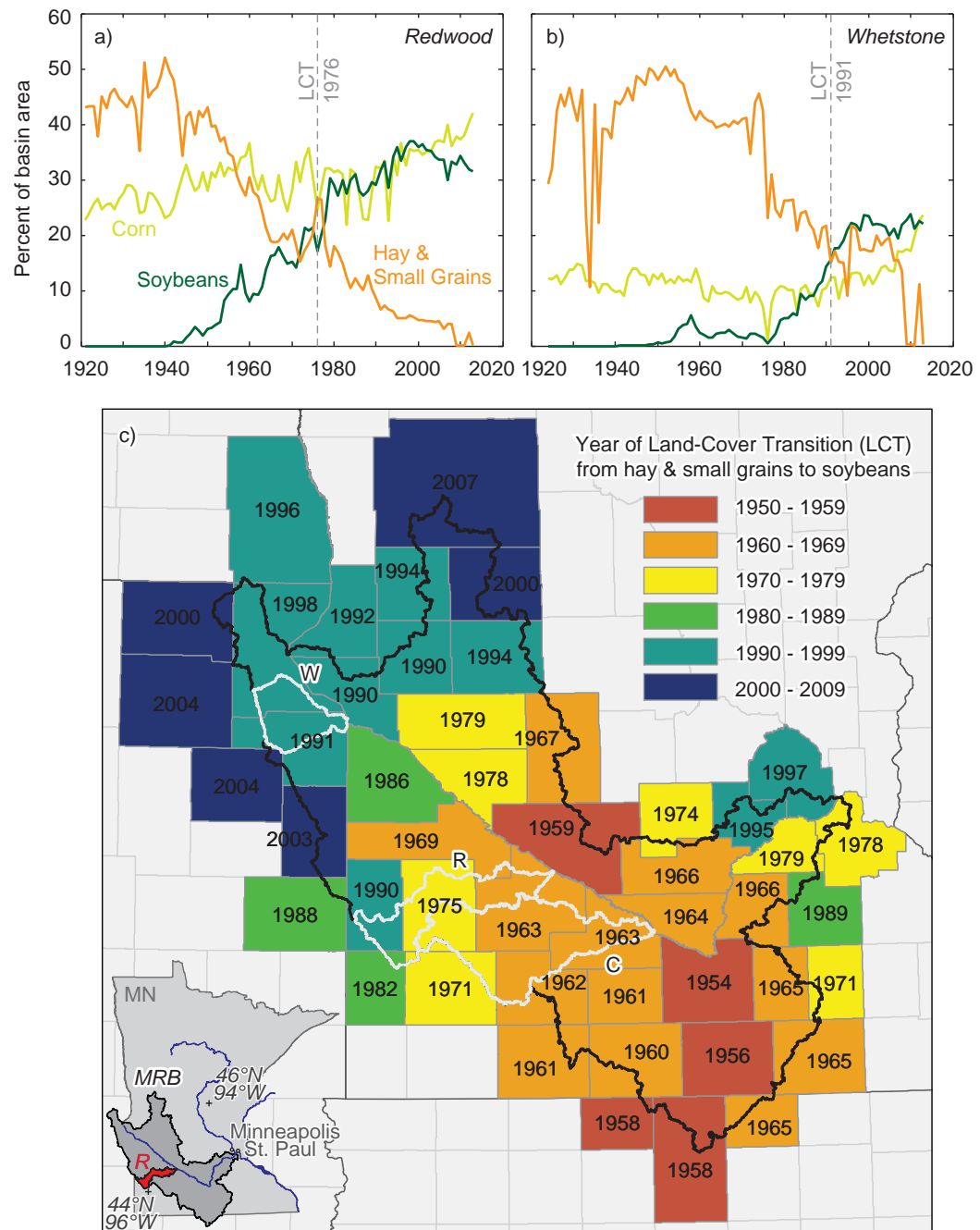


Figure 2. Spatial progression of agricultural changes in the Minnesota River Basin (MRB). Using land-cover data at the county level, we define the “Land-Cover Transition” (LCT) as the year when the percentage of area for growing soybeans exceeded that for hay and small grains (barley, flax, oats, rye, and wheat) (see examples in (a) Redwood and (b) Whetstone basins). (c) The map demonstrates the southeastern to northeastern progression of this agricultural transition. The Redwood (R), Cottonwood (C), and Whetstone (W) subbasins are shown for reference. Data are from the U.S. Department of Agriculture National Agricultural Statistics Service [USDA, 2014].

which the HT may occur. However, the HT for a basin may occur after the 1970s if the LCT has not yet occurred.

Figure 3 establishes a link between agricultural and hydrologic change by focusing on the daily streamflow series of three river basins (see map in Figure 2) during only the growing season of May–June when tile drainage is most active and climate effects are minimal. For the Redwood basin (1800 km^2), the LCT in 1976 (Figure 3a) synchronizes well with the HT (Figure 3b) corresponding to the onset of major hydrologic change. The Cottonwood basin (3400 km^2) undergoes its LCT in 1964 (Figure 3c), but its HT does not occur

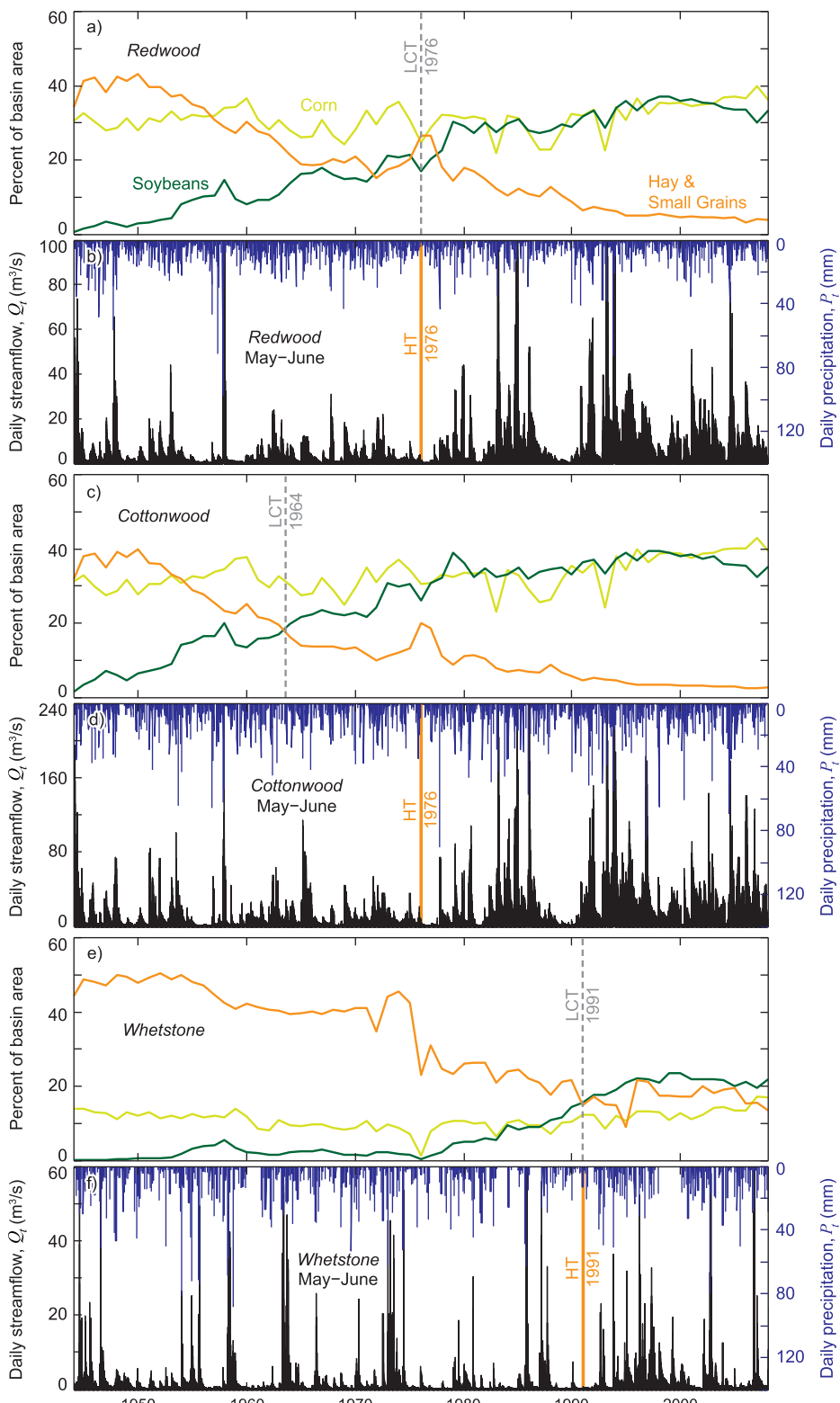


Figure 3. The imprint of agricultural land use change on hydrologic change. Using daily streamflow data in the growing season of May–June to minimize climatic effects, the onset of hydrologic change is observed following the conversion to soybeans, i.e., following the Land-Cover Transition (LCT), which was objectively extracted from land-cover data for each basin (see also Figure 2). A lower bound on the HT can be set based on the 1970s or LCT, whichever occurred later. Here we adopt the mid-1970s (1976) as the HT year for Redwood and Cottonwood basins. We caution that adopting the same year for all basins can be misleading—for Whetstone, for example, selection of 1976 would certainly mask hydrologic change.

until the 1970s (Figure 3d) since the HT requires both predominant soybean cover (LCT) and the technological tile advances of the 1970s. In the Whetstone basin (1100 km^2), the LCT in 1991 (Figure 3e) occurred well after the 1970s, and its HT was correspondingly delayed until 1991 (Figure 3f). These examples suggest that each basin's agricultural development must be considered independently, as using the mid-1970s as the HT year for the Whetstone basin would be misleading and mask hydrologic changes.

3. The Nature of Hydrologic Change

In this section, we examine in detail the hydrologic changes in the Redwood River basin. Daily streamflow data were obtained from the USGS streamflow gage at Redwood Falls (05316500) [U.S. Geological Survey, 2014], and three NOAA precipitation stations (Marshall, Tyler, and Vesta) [National Oceanic and Atmospheric Administration, 2015] were used to compute the daily average precipitation over the basin. These stations are displayed in Figure 4 together with the detailed land cover of the basin in 2007 and a demonstration of the corn-soybean rotation for a small inset of the basin. Using the previously established HT year of 1976 for this basin, we separate the series into Before Land Use Change (BLUC) and After Land Use Change (ALUC) periods.

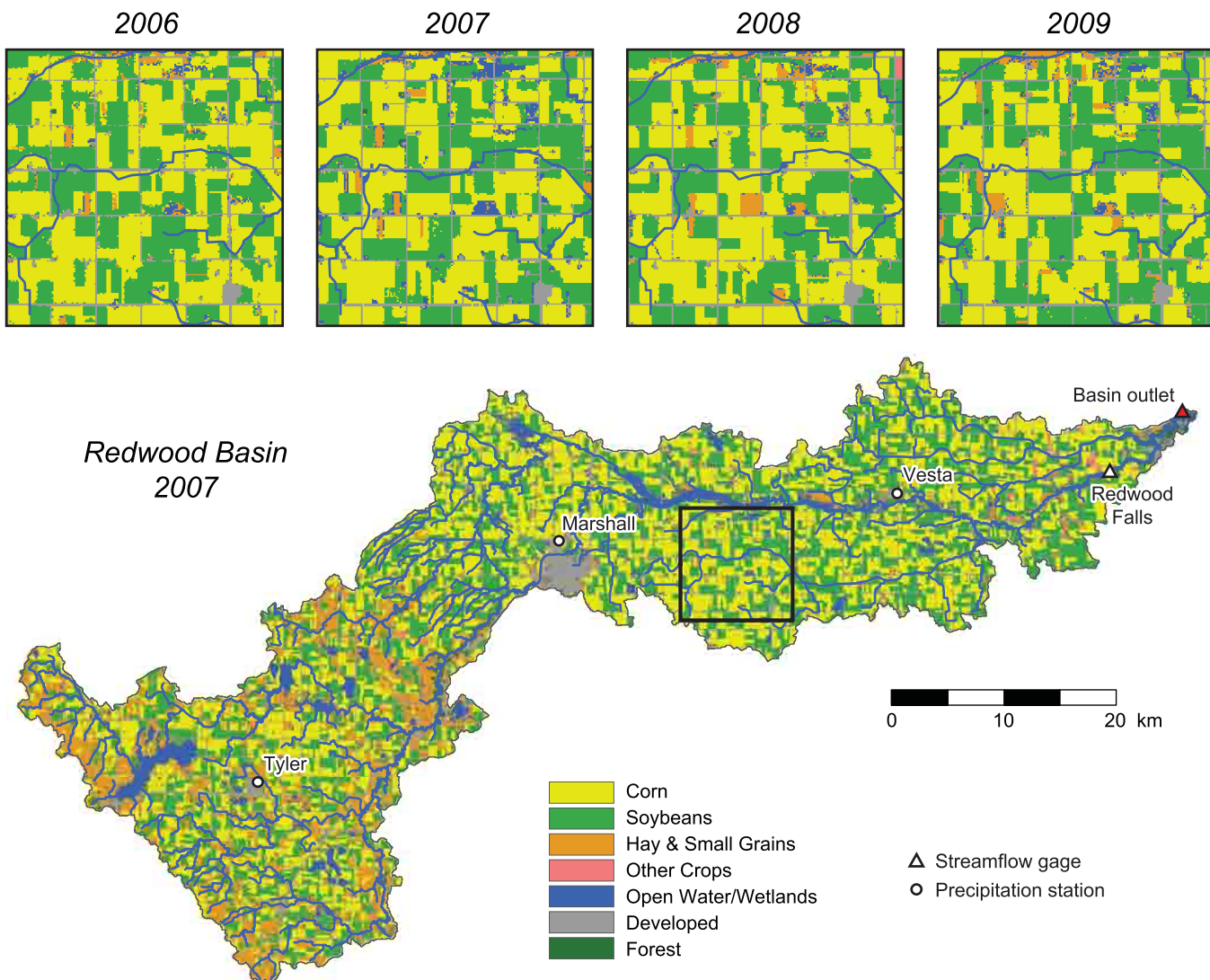


Figure 4. The 2007 land-cover data of the 1800 km^2 Redwood basin show that the majority of the basin is cultivated with corn and soybeans [U.S. Department of Agriculture, 2015]. An inset box showing the same area for four different years 2006–2009 illustrates typical crop rotation between corn and soybeans from one year to the next.

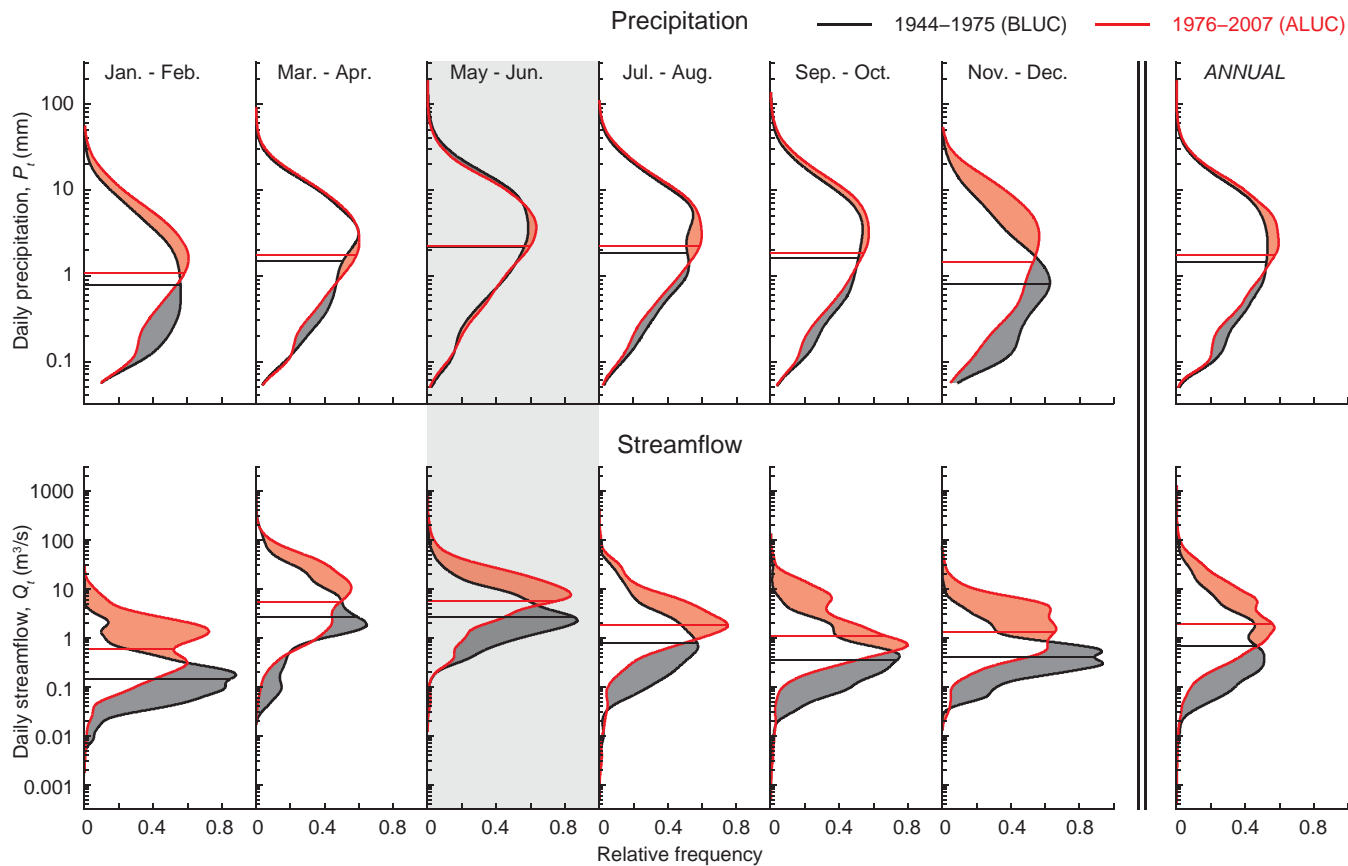


Figure 5. Probability distribution functions (pdfs) of daily precipitation and streamflow for 2 month and annual periods for the Redwood basin for BLUC (1944–1975; black) and ALUC (1976–2007; red). The horizontal line denotes the mean, and the shading highlights the difference between the pdfs. The May–June growing season is shaded demonstrating minimal precipitation change but significant streamflow change. Pdfs of daily streamflow consistently shift to larger values in all months of the ALUC period. The hydrographs in the May–June period have been analyzed via Copulas as shown in Figure 6.

3.1. Hydrologic Response Change During the Growing Season

Streamflow statistics for the Redwood basin reveal that daily streamflow has increased in all months ALUC, whereas daily precipitation has not changed much except for increases during November–February (Figure 5). During March–April, streamflow is affected by both snowmelt whose onset is occurring earlier due to higher temperatures [Walsh et al., 2014] and agricultural drainage. By May, snowmelt is no longer a major factor and agricultural activity takes over as crops have been planted and agricultural drainage is most active due to fields saturated with snowmelt and spring rainfall. During the growing season of May–June, changes in the probability distribution of daily precipitation were not significant while drastic changes in hydrology were observed (Figure 5). We note that an analysis of storm totals, durations, and interarrival times (not reported here) did not provide evidence for change in the ALUC period. Changes in hydrologic response, then, may be attributed to nonclimatic effects including the predominant agricultural land use changes.

To quantify changes in hydrologic response, we jointly analyzed streamflow Q_t , streamflow increments, $dQ_t/dt = (Q_{t+1} - Q_t)/\Delta t$, and precipitation P_t to detect possible changes in their probabilistic dependence. Specifically, we analyzed (1) positive streamflow increments ($dQ_t/dt > 0$) or rising limbs of daily hydrographs, dQ_t^+/dt , against precipitation, P_t , and (2) absolute value of negative streamflow increments ($dQ_t/dt < 0$) conditioned on no precipitation the previous day, $dQ_t^-/dt|P_t=0$, against streamflow, Q_t . The first relationship (dQ_t^+/dt versus P_t) captures how daily precipitation is converted to daily streamflow via the “unaltered” (BLUC) and human-altered (ALUC) hydrologic connectivity system. Strengthened overall dependence of the hydrograph slope on precipitation in the ALUC May–June period was expected due to the direct subsurface drainage, but the nature of the dependence was seen through an interquantile dependence analysis. The probabilistic dependence of $dQ_t^-/dt|P_t=0$ versus Q_t captures the rate of hydrograph decline in the absence of rain as a function of streamflow and changes would reflect altered storage-discharge dynamics. In order to

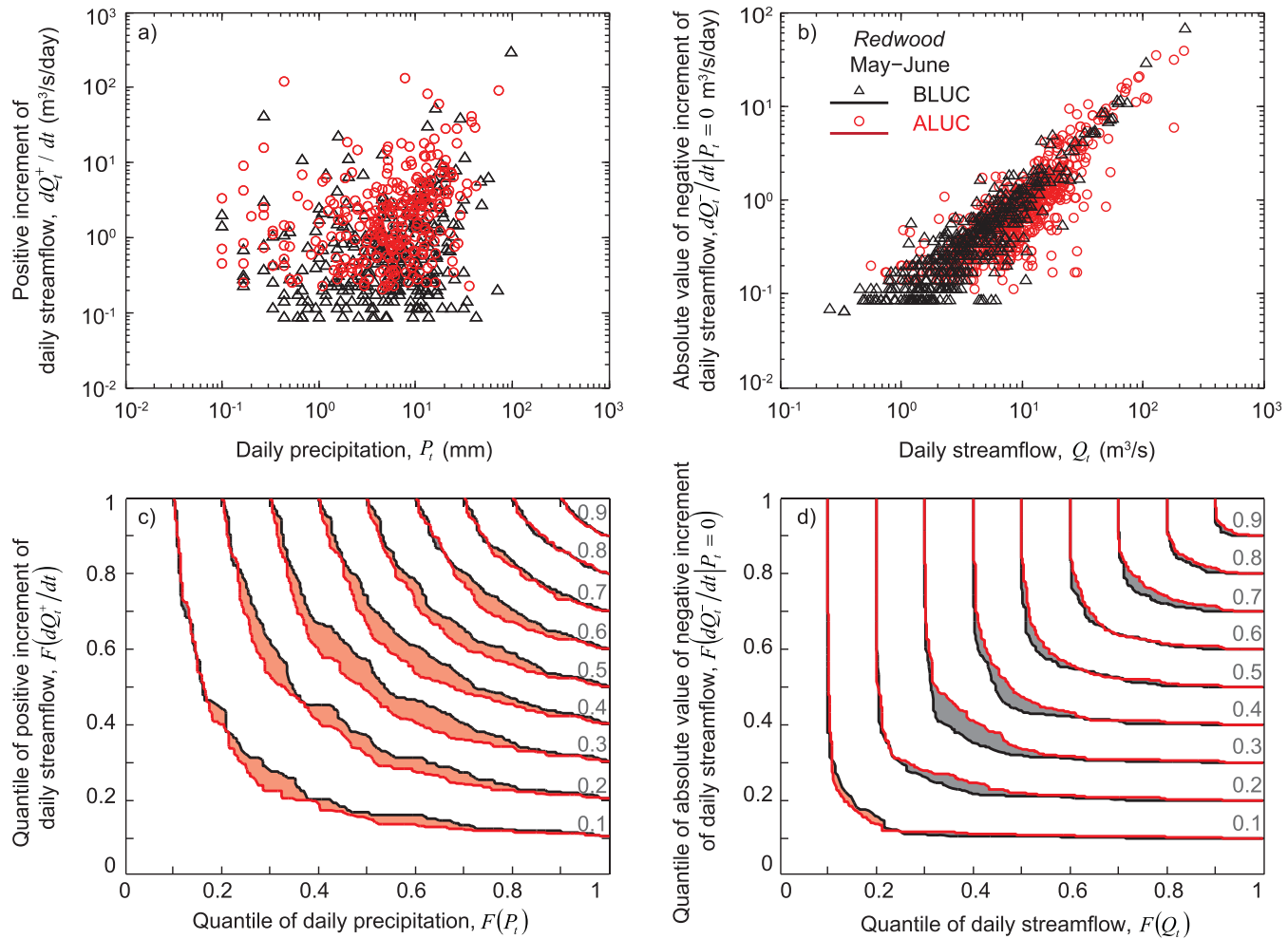


Figure 6. Copula interquantile analysis of hydrologic response for the BLUC (black) and ALUC (red) periods of the Redwood basin. (a) Scatterplot of positive slopes of daily hydrographs dQ_t^+ / dt versus previous-day precipitation P_t . (b) Scatterplot of negative slopes of daily hydrographs dQ_t^- / dt conditioned on no previous-day rainfall ($P_t = 0$) versus streamflow Q_t . (c) Copula of dQ_t^+ / dt and P_t . (d) Copula of $dQ_t^- / dt|P_t=0$ and Q_t . A strengthened dependence of streamflow increase to previous-day rain (a and c) and a reduced dependence of the falling hydrograph slope to streamflow magnitude (b and d) are observed in the ALUC period. See text for discussion.

focus on the structure of flood hydrographs, very small increments of streamflow were not considered here as these were found to correspond to base flow and isolated fluctuations in the hydrograph limbs. By varying the threshold and examining the location of these fluctuations, we chose the truncation level of 0.2 quantile corresponding to $dQ_t^+ / dt < 0.08 \text{ m}^3/\text{s}$ ($0.20 \text{ m}^3/\text{s}$) and $|dQ_t^- / dt| < 0.06 \text{ m}^3/\text{s}$ ($0.11 \text{ m}^3/\text{s}$) for BLUC (ALUC) periods.

We employed nonparametric Copula analysis [Favre et al., 2004; Dupuis, 2007; Salvadori and De Michele, 2007; Rüschenhoff, 2009] to quantify how the dependencies discussed above changed between BLUC and ALUC periods. The Copula is defined as the joint cumulative distribution of the quantiles of two random variables and contains all the information of their dependence. Let X_1 and X_2 denote two random variables with marginal cumulative distributions $F_1(x_1) \equiv P[X_1 \leq x_1]$ and $F_2(x_2) \equiv P[X_2 \leq x_2]$ and cumulative joint distribution function $F(x_1, x_2) \equiv P[X_1 \leq x_1, X_2 \leq x_2]$. Sklar's theorem [Nelsen, 1999] relates the joint distribution $F(x_1, x_2)$ of X_1 and X_2 to the cumulative distribution function $C(u_1, u_2)$ of the quantiles $u_1 = F_1(x_1)$ and $u_2 = F_2(x_2)$ by:

$$\begin{aligned} F(x_1, x_2) &= P[X_1 \leq x_1, X_2 \leq x_2] \\ &= P[X_1 \leq F_1^{-1}(u_1), X_2 \leq F_2^{-1}(u_2)] \\ &\equiv C[U_1 \leq u_1, U_2 \leq u_2] = C(u_1, u_2) \\ &= C(F_1(x_1), F_2(x_2)) \end{aligned} \quad (1)$$

where $C(F_1(x_1), F_2(x_2))$ is the Copula.

Empirical Copulas $C(F(dQ_t^+/dt), F(P_t))$ and $C(F(dQ_t^-/dt|P_t=0), F(Q_t))$ are shown in Figures 6c and 6d, where the axes values show the marginal quantiles of each variable and the curves trace the cumulative Copulas at varying quantile levels. An “L-shaped” Copula implies a larger interquantile dependence between the two variables. As expected, the empirical Copula of the flashiness of the hydrograph $C(F(dQ_t^+/dt), F(P_t))$ shows a strengthened dependence structure in ALUC (Figure 6c) establishing that the rate of increase in streamflow (dQ_t^+/dt) in response to the previous-day precipitation has become more closely coupled across a range of quantiles, especially for medium (0.2–0.6) quantiles for both variables. This tighter probabilistic dependence is also visible in Figure 6a, although no inference about quantile dependence can be easily made from such a plot.

The empirical Copula of the falling limbs of the hydrographs $C(F(dQ_t^-/dt|P_t=0), F(Q_t))$ did not show as significant a change in the dependence structure of the rate of decrease of the falling limb to the magnitude of streamflow from BLUC to ALUC (Figure 6d). If anything, this dependence has weakened in the ALUC period as the Copula curves have become less L shaped, especially in the medium quantiles. Interpreting this dependence weakening is not straightforward, but examination of multiple individual hydrographs revealed that in ALUC the falling limbs of the hydrographs have become more “punctuated.” That is, for a value of Q_t of some exceedance probability, the corresponding slope dQ_t^-/dt became more variable in the ALUC period (Figure 6b). Apparently, in this basin, artificial drainage accelerates the hydrologic response at smaller scales, maintaining rather than integrating the signature of the subbasin contributions to the outlet of the larger basin. Hydrographs from the now-faster draining smaller subbasins in the ALUC period maintain separation from each other when routed through the river system due to the discrepancy between the small subbasin hydrograph time scales and river routing time scales. This creates a rougher overall falling hydrograph limb at the outlet of the larger basin. It remains to be understood further how this effect depends on the scale of the basin and whether it reflects more the overall basin heterogeneity or its hierarchical drainage structure [e.g., see Harman et al., 2009; Chen and Krajewski, 2015].

Understanding a basin’s hydrologic response through analyzing receding hydrograph slopes dQ_t^-/dt has a long history. For example, Brutsaert and Nieber [1977] used the lower envelope of the dQ_t^-/dt versus Q_t relationship to interpret the recession curves from a hydraulic perspective and guide regionalized prediction of drought hydrographs in ungauged basins. Kirchner [2009] proposed using the dQ_t^-/dt versus Q_t relationship for catchment characterization via a catchment storage function. Harman et al. [2009] provided a landscape interpretation of the recession curves as capturing landscape heterogeneity, Biswal and Marani [2010] linked recession curve properties to river network morphology, and Chen and Krajewski [2015] accounted for the hierarchical (nonrandom) organization of landscapes and the scale effect of the storage-discharge relationship. Shaw and Riha [2012] investigated individual recession events within the dQ_t^-/dt versus Q_t cloud of points, noting that much of the scatter arose from seasonal variability. Here we explored the (dQ_t^-/dt versus Q_t) and (dQ_t^+/dt versus P_t) relationships from a probabilistic dependence perspective and specifically to assess whether a change occurred in the precipitation-to-streamflow conversion and in the storage-discharge relationship. To the best of our knowledge such analysis has not been reported before and its potential for detecting hydrologic change deserves further investigation.

3.2. Change in Daily Streamflow Dynamics

Agricultural drain tiles short-circuit natural recharge processes not only during the growing season but also in the summer and during the snowmelt periods. This land-use imposed change superimposed on climatic changes creates an altered daily streamflow signal throughout the entire year. Figure 7a displays the year-long series of daily precipitation and streamflow for the Redwood basin from 1944 to 2007, whereas Figures 7b and 7c display the squared modulus of the Morlet wavelet coefficients $|T(a, b)|^2$ giving the relative contribution of the signal’s energy at different scales a and locations b (see Appendix A for details on wavelet selection and implementation). Amplified energy content is observed in all scales of streamflow over the last two decades (Figure 7c), while little change is observed in daily precipitation (Figure 7b).

To quantify changes in the underlying dynamics of daily precipitation and streamflow, we tapped into the theory developed for deterministic nonlinear systems and invoked the acclaimed Takens theorem [Takens, 1981] for embedding a data series into an appropriately chosen phase space. The embedding procedure results in a geometric representation of the system’s dynamics called an attractor (see Appendix B for details). Measures on reconstructed attractors from BLUC and ALUC periods quantified the magnitude and

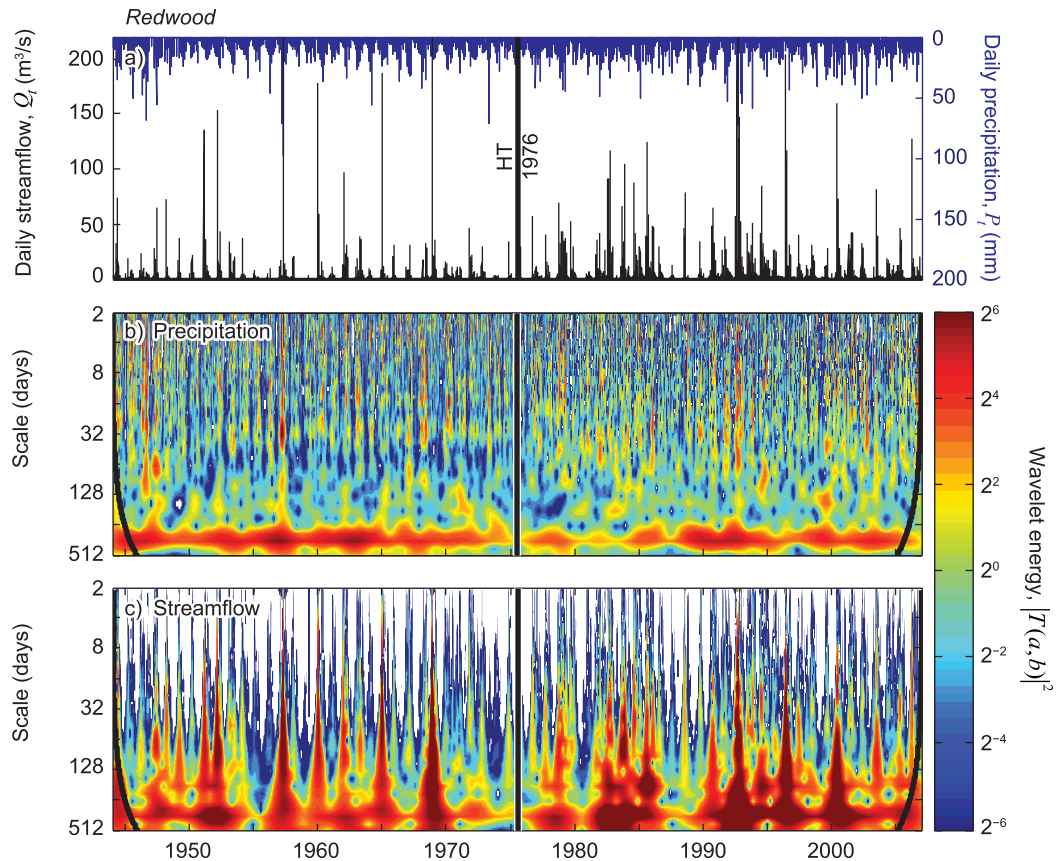


Figure 7. Temporal change in precipitation and streamflow in the Redwood basin. (a) Daily precipitation and streamflow series and (b and c) time-frequency plots using Morlet wavelet. The Hydrologic Transition (HT) year of 1976 (see Figure 3) is marked.

abruptness of the shift in the underlying dynamics of daily precipitation and streamflow. Beyond just capturing changing streamflow dynamics, we also measured the degree of nonlinearity in the dynamics of BLUC and ALUC conditions. To detect progressive changes in the dynamics of daily streamflow and precipitation, the BLUC and ALUC periods were further subdivided into two time periods of equal length for a total of four series: BLUC1, BLUC2, ALUC1, and ALUC2. A brief account of the essence of the nonlinear analysis carried out on daily streamflows and precipitation follows, and a more detailed description may be found in Appendix B.

If two time series are properly embedded in the same phase space, their resulting attractors may contain structural and density differences reflecting differences between their underlying dynamics. Among a number of metrics to measure such differences, the transportation distance d_T [Kantorovitch, 1958] considers both geometric and probabilistic attractor structure while being insensitive to outliers, perturbations, and discretization errors (see Appendix C and Moeckel and Murray [1997] for comparisons against other similar distance metrics).

Each period BLUC1, BLUC2, ALUC1, and ALUC2 was embedded into a rigorously determined phase space of dimension three (four) and lag 20 (10) days for streamflow (precipitation); see Appendix B and Schreiber [1999]. Then, the distance metric d_T was computed between each pair of attractors (Figure 8). Larger d_T indicates significant discrepancy between attractors and implies a difference in the generative dynamical systems. Streamflow attractors between BLUC1 and BLUC2 were more alike than any other pair, implying their dynamical systems are correspondingly most similar. According to Figure 8b, the hydrologic dynamics of the basin shifted substantially between BLUC2 and ALUC1, supporting the choice of 1976 as a hydrological transition year for the Redwood basin. Dynamics continued to shift between ALUC1 and ALUC2 periods. Although hydrologic changes were likely occurring throughout the entire period of record, if the conservative assumption of unchanging dynamics between BLUC1 and BLUC2 is granted, then $d_T = 0.73 \times 10^{-3} \text{ m}^3/\text{s}$ provides a measure of variation expected due to noise, discretization effects, etc. The fact that d_T obtained significantly

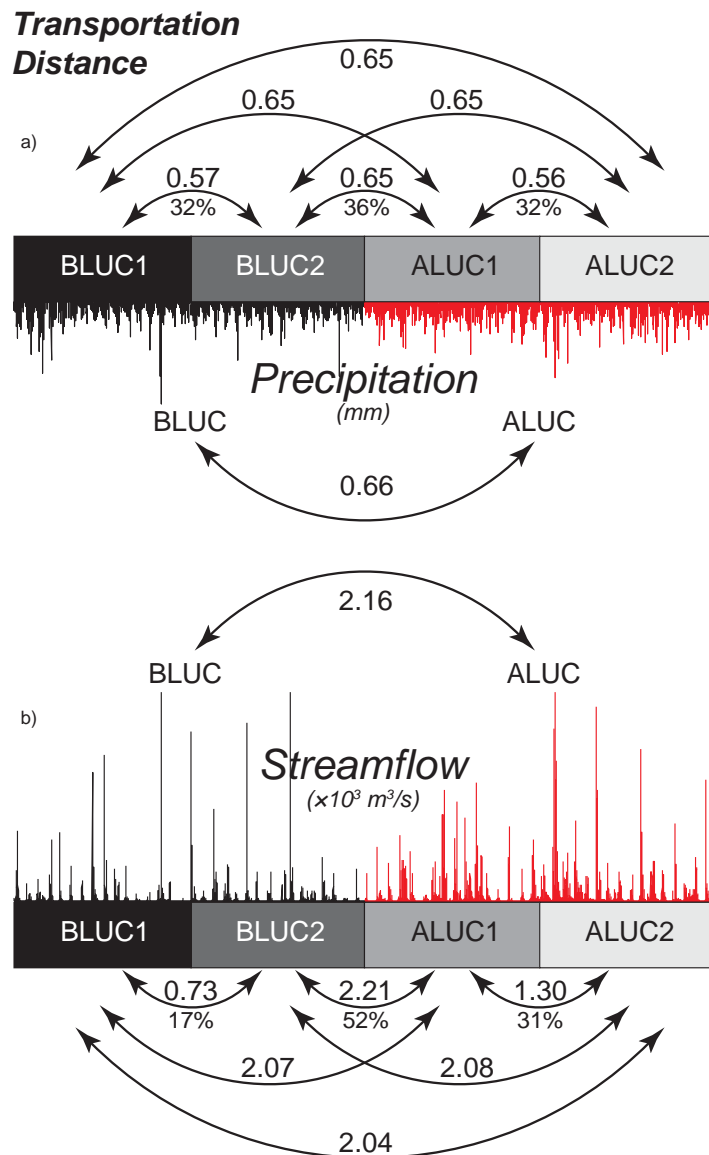


Figure 8. Change in nonlinear dynamics of daily precipitation and streamflow. Transportation distances are shown between the attractor pairs of (a) precipitation and (b) streamflow between four time periods described in section 3.2. Precipitation and streamflow series are plotted from 1944 to 2007; BLUC in black and ALUC in red. Percentages are computed for the three chronological distances as d_T divided by the sum of d_T between all three distances. Clearly precipitation dynamics have not changed significantly but streamflow dynamics have.

original signal and its linear variants (OS_i), as well as the distances between the linear variants amongst themselves (SS_j), resulting in two distributions: $d_{T,OS}$ and $d_{T,SS}$ (Figure 9). A larger distance between the $d_{T,OS}$ and $d_{T,SS}$ distributions implies that the original signal contained more nonlinearity that was destroyed by the linearization procedure. Therefore, nonlinearity may be inferred if these distributions are significantly nonoverlapping. On the other hand, for example, distributions from an ARMA-generated time series are entirely overlapping. The difference between the medians of $d_{T,OS}$ and $d_{T,SS}$ may thus be taken as a measure of nonlinearity.

Transportation distances between original signals and linear surrogates for BLUC and ALUC showed that streamflow dynamics have become more linear post-1976 (Figure 9b). This result is arguably consistent

higher values through time indicates an accelerated shift in hydrologic dynamics post-1976. In contrast, precipitation dynamics showed much less change (Figure 8a). Unfortunately however, precipitation and streamflow transportation distances were not directly comparable; each has units of its input data and d_T scales with discretization schemes. However, normalization of d_T from the three chronological pairs by their sum (percentages in Figure 8) suggested that changes in streamflow dynamics are not likely attributable to nonstationary precipitation alone, as relative differences between precipitation d_T were much smaller than those between streamflows.

The nature of an altered dynamical system's change may be further understood by measuring its attractor's degree of nonlinearity. A signal's nonlinearity may be quantified by first generating linearized versions of the series known as surrogates. Inherent nonlinearities in the original signal are destroyed in the surrogates via phase randomization in the Fourier domain while preserving the power spectrum, distribution, and linear correlation structure of the original series. We employed the Wavelet-modified Iterated Amplitude Adjusted Fourier Transform [Keylock, 2008] algorithm for surrogate generation. The transportation distance then measures the distances between the

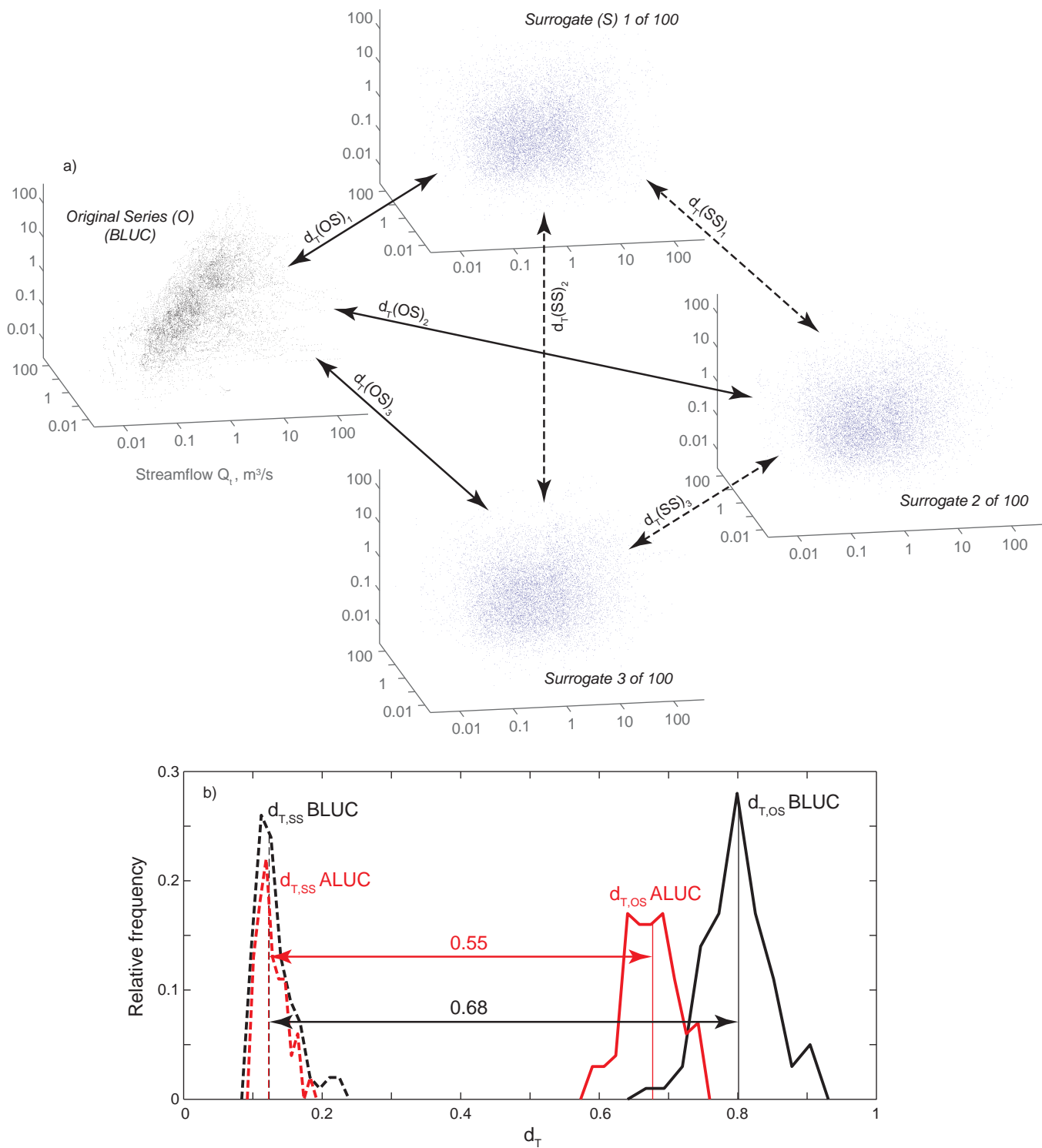


Figure 9. Quantifying the degree of nonlinearity in daily streamflow series. (a) Log-transformed attractors of streamflow are shown for the original BLUC series (black) and linearized surrogates (blue). A total of 100 surrogates were generated, and the transportation distance between each surrogate and the original signal $d_T(OS)$ is shown by solid arrows. Transportation distances between 100 surrogate pairs $d_T(SS)$ are shown by dashed arrows. (b) Distributions of d_T between original signal and 100 surrogates ($d_T(OS)$) are shown by solid lines. Distributions of d_T between 100 pairs of surrogates ($d_T(SS)$) are shown by dashed lines. The differences between the medians of $d_T(OS)$ and $d_T(SS)$ are shown for BLUC (black) and ALUC (red) conditions. These results quantify the reduced nonlinear dynamics in the ALUC period.

with the intuition that engineered landscapes introduce an element of “simplicity” in the water system (e.g., Schilling and Helmers [2008] report that tiling results in more linear base flow recession curves). Identifying which portions of the daily streamflow record contributed most to reduction of inherent

nonlinearity is not straightforward using the methods described here, although such inquiry could be undertaken using the Gradual Wavelet Reconstruction methodologies of Keylock [2010].

4. The Nonlinear Cascade of Hydrologic Change to Regime Shifts in River Ecology

4.1. A Simplified Interaction Model Coupling Hydrology and River Ecology

Decline in native mussel, macroinvertebrate, and sensitive fish species populations [Kirsch *et al.*, 1985; Musser *et al.*, 2009] coincident with changes in land use, hydrology, climate, and sedimentation [e.g., Kelley and Nater, 2000; Engstrom *et al.*, 2009; Belmont *et al.*, 2011] in the Minnesota River Basin call for an understanding of the couplings between hydrology, geomorphology, and ecology to guide assessment of future states. A model recently proposed by Hansen *et al.* [2015] considers the interactions between streamflow (Q_t), suspended sediment (S_t), phytoplankton population density (chlorophyll-a) (C_t), and mussel population density (M_t) (Figure 10a). Three coupled differential equations driven by hydrology (see equations (D1)–(D3)

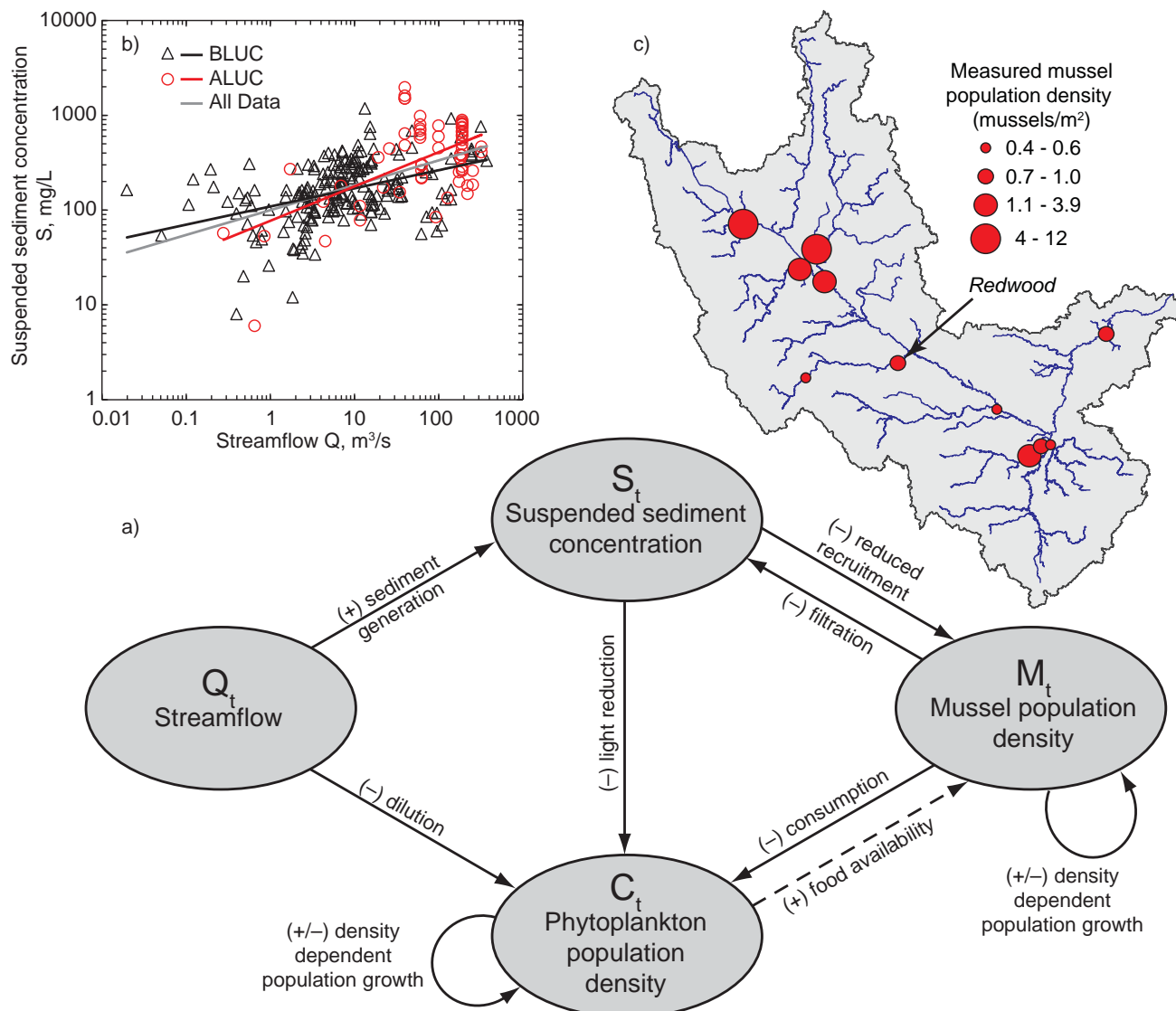


Figure 10. Overview of simulated mussel population dynamics driven by streamflow. (a) Schematic of the process interaction network showing the couplings incorporated in the mussel population density model. Each arrow represents a physical interaction considered by the model which is either positive (+) or negative (−). (b) Flow-sediment relationship from USGS gaging station data with power law fits for BLUC ($n = 207$), ALUC ($n = 67$), and all data. α, β values for each period: BLUC (29.1, 0.191), ALUC (6.36, 0.362), and all data (16.4, 0.262). (c) Map of the Minnesota River basin showing the sites (red circles) with observed mussel population densities where the model of Hansen *et al.* [2015] was applied. The analysis herein focuses on the Redwood site indicated by the arrow.

in Appendix D) predict site-specific mussel population abundance. The model was fitted and calibrated at 11 sites within the MRB where mussel abundance data were available, and it can be used as a predictive or diagnostic tool to explore how changes in hydrology and/or sediment production propagate to river ecology. Details can be found in Hansen *et al.* [2015].

Here we employed this model at the Redwood site (at Redwood Falls)—a site with low mussel abundance—to investigate how daily streamflow change nonlinearly modulates suspended sediment generation and food availability, thus determining the future of the mussel population density and its possible decline or even extirpation. Mussel population dynamics are governed by a logistic-type model:

$$\dot{M}_t = r_t M_t \left(1 - \frac{M_t}{\eta_t K_M} \right) \quad (2)$$

where the dot in \dot{M}_t denotes the time derivative of the mussel population M_t at time t . The mussel growth rate parameter r_t depends on the suspended sediment concentration (S_t), and η_t reduces the carrying capacity K_M when food (C_t) becomes scarce, resulting in an effective carrying capacity $\eta_t K_M$.

Assuming constant parameters r_t and η_t , equation (2) has two fixed points (i.e., equilibrium states, or where $\dot{M}=0$) corresponding to population extirpation ($M^*=0$) and effective carrying capacity ($M^*=\eta_t K_M$). Given sufficient time, then, mussel populations will either wither or thrive depending on the sign of the RHS of equation (2). Specifically, when $r_t > 0$, a population grows toward its effective carrying capacity and when $r_t < 0$ a population diminishes toward extirpation. The formulation of r_t results in the following condition:

$$\begin{array}{ll} \text{if } S_t < S_{thresh} & r_t > 0 \\ S_t > S_{thresh} & r_t < 0 \end{array} \quad (3)$$

where S_{thresh} represents a threshold level of suspended sediment above which mussel birth rate becomes smaller than the mortality rate, resulting in population decline. S_{thresh} depends on model parameters and for the Redwood site equals 18.9 mg/L [see Hansen *et al.*, 2015].

The deterministic model dynamics are forced via stochastic streamflows Q_t . Because of this, r_t and η_t are generally not constant as assumed above, and therefore fixed point stabilities also vary in time. Phase portraits and stability landscapes well-illustrate fixed point stability; the phase portrait (Figure 11a) simply plots \dot{M}_t (equation (2)) for all realistic values of M , and the stability landscape (Figure 11b) intuitively conceptualizes population dynamics as an inertia-less ball rolling down a hill (see Appendix E for formulation and details). Nonstationarity of r_t and η_t implies that each time may have a unique phase portrait and stability landscape. Fixed point stability depends solely on the sign of r_t . That is, for $r_t > 0$, $M^*=0$ is unstable and $M^*=\eta_t K_M$ stable. For $r_t < 0$, the stabilities of the fixed points flip. As discussed above, the sign of r_t depends on S_t , thus population stability depends on S_t . The parameter η_t depends on available food (C_t) and acts to stretch both the phase portrait and stability landscape (stretching between gray and black curves of the same line type in Figures 11a and 11b).

The outermost phase portraits in Figure 11a delineate the model's accessible dynamic space; these portraits correspond to low S_t ($\max(r_t)$) associated with lower Q_t and large S_t from flood flows ($\min(r_t)$). Since C_t is also modeled semilogistically, it has fixed points $C^*=[0, \eta_C K_C]$ which correspond to $\eta_t=[0.5, 1]$. Therefore, simulated mussel populations tend to evolve according to one of the four phase portraits shown in Figure 11a. The phase portrait also shows that for a given M , population declines at a time can be roughly 3 times larger in magnitude than growths (Figure 11a). This feature is also visible in the time series of M_t (Figure 12a)—a dynamic suggesting that a population for which $S_t > S_{thresh}$ above roughly 25% of the time will eventually approach extirpation.

4.2. Effects of Hydrologic Change on Mussel Populations

In this section, we explore how the observed hydrologic changes may propagate to ecologic changes and elucidate emergent critical regime transitions. Consistent with the land use change (section 2) and statistical and nonlinear streamflow analyses (section 3), the year 1976 was selected to separate two distinct hydrologic regimes to apply to mussel populations at the Redwood site: BLUC (1944–1975) and ALUC (1976–2007). The volume of suspended sediment generated from a given discharge may also vary with hydrological or morphological changes. For instance, a river migrating across its flood plain and into bluffs may result

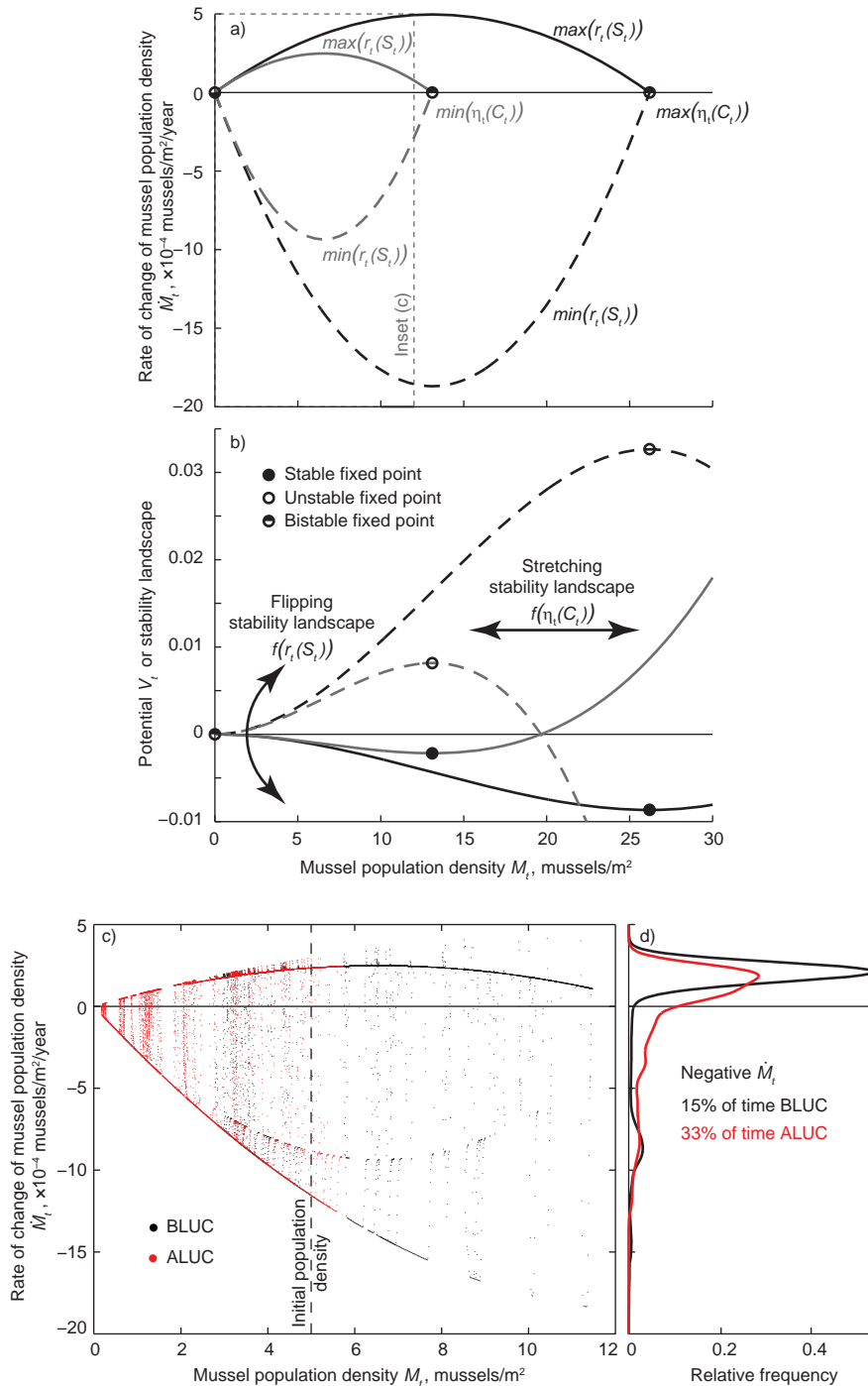


Figure 11. Nonlinear dynamics of the mussel population model. (a) Phase portraits show the possible dynamic space visited by model dynamics. Each portrait has two fixed points $M^* = 0, \eta_t K_M$ whose stabilities depend on the sign of r_t . For positive r_t , portraits are above zero (solid lines) with stable fixed points at $M = \eta_t K_M$. Negative r_t (dashed lines) corresponds to stable fixed points at $M = 0$. The stretching of each portrait is determined by η_t , which ranges from 0.5 to 1. (b) Stability is visualized as a ball rolling down stability landscapes. Like in Figure 11a, r_t controls the orientation and η_t stretches the landscape. See Appendix E for details. (c) A phase portrait of mussel population density shows the effects of hydrology on model dynamics. Each dot represents the modeled mussel population density (x axis) and its corresponding change (y axis) for each day over 32 years starting from an initial population density of 5 mussels/m². Only input streamflows are different between the ALUC and BLUC conditions above; all other model parameters including the flow-sediment relationship are identical. Populations under ALUC hydrology move toward extirpation, while BLUC hydrology results in a population approaching effective carrying capacity. (d) PDFs of daily population growth rates shown in Figure 11c. The 85% of BLUC time steps result in population growth, compared to only 67% for ALUC conditions.

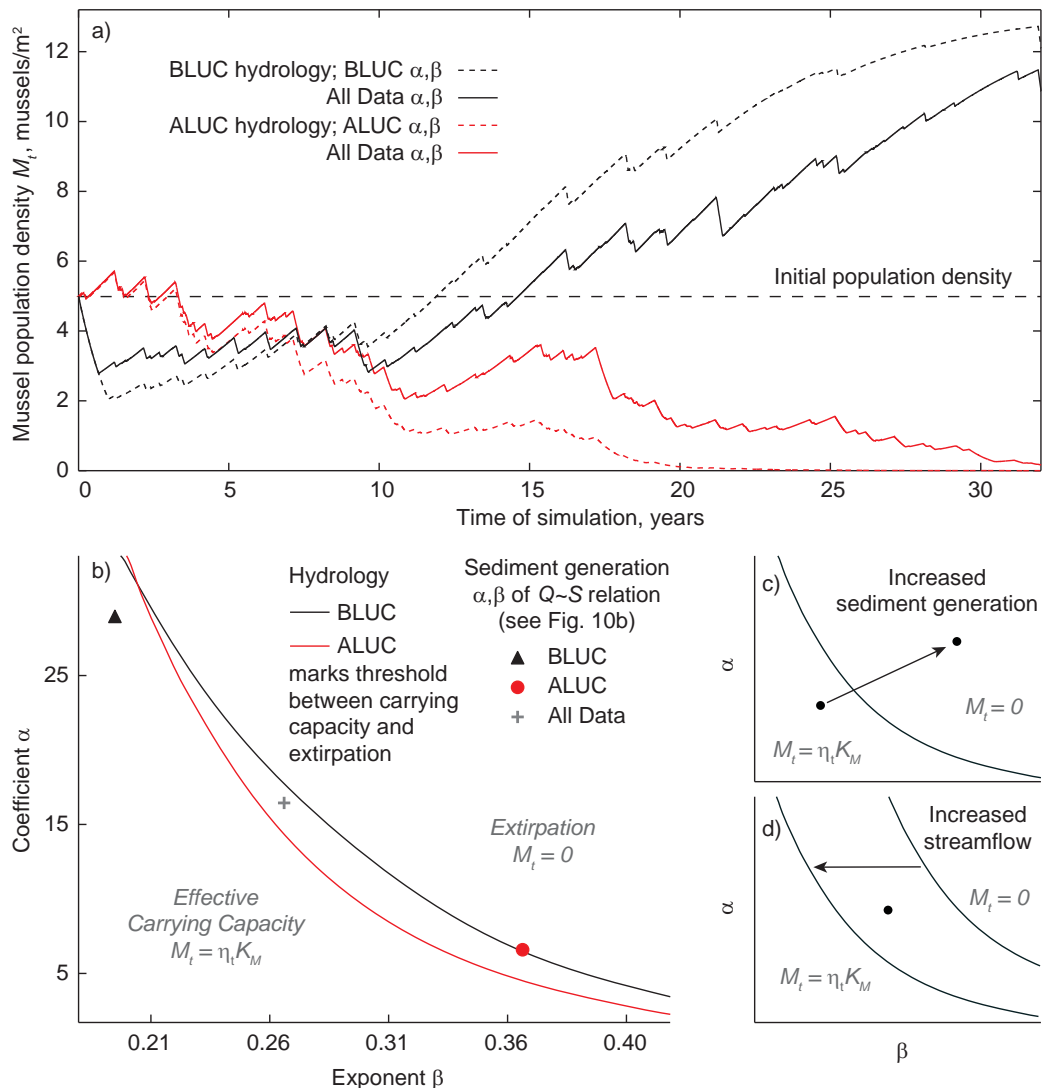


Figure 12. Mussel population stability as a function of hydrology and sediment generation. (a) Mussel population densities are simulated for 32 years driven by hydrology BLUC (black lines) and ALUC (red lines). For each hydrology, populations were simulated using the flow-sediment relationship of the respective period (dashed lines) and the relationship derived from the entire record (solid lines). (b) Population stability diagram for the Redwood site. Regime transition lines depend on observed hydrology, while positioning in the space depends on the (α, β) fits to observed data (Figure 10b). Points above a given line correspond to (α, β) pairs that result in extirpation as the stable fixed point, while those below have a stable fixed point at the effective carrying capacity. Points far away from the line reach steady state faster than those nearer the line (see (a)). (c) Fixed point stability may switch due to changes in sediment generation or (d) changes in hydrology.

in larger sediment supplies for a given flow. On the other hand, bank stabilization measures and riparian corridors may reduce sediment loading to streams. These effects are captured by the parameters α, β of the power law fits to suspended sediment against streamflow data, which were performed for BLUC, ALUC, and all data (Figure 10b).

As discussed above, simulated mussel populations approach one of two possible steady states: extirpation or effective carrying capacity. Since population decay occurs when $S_t < 18.9 \text{ mg/L}$, and $S_t = f(Q_t)$, both streamflow (Q_t) and sediment generation parameters α, β play crucial roles in a population's final state. Even if sediment generation is assumed constant, increased streamflow alone may switch a population's stable fixed point from a healthy population to extirpation (Figure 12d). Conversely, sediment generation may also cause a regime shift even if streamflow remains unchanged (Figure 12c).

Observed mussel population density at the Redwood site is among the lowest in the MRB (Figure 10c). We simulated mussel population densities across a range of realistic α, β values using repeated BLUC or ALUC

streamflows until populations reached a steady state. Realistic values obtained from the values at 10 other sites across the MRB ranged from $(\alpha, \beta) = (0.22, 0.24)$ to $(16, 0.63)$. The resulting α, β space can then be divided by a line demarcating the critical threshold for a regime transition that is determined by the applied hydrology; above this line, populations are extirpated, and below this line, populations reach their effective carrying capacity. This space for the Redwood site (Figure 12b) tells a compelling story. Conservatively consider that sediment generation remained constant across both BLUC and ALUC periods (gray "+" symbol). In this case, altered hydrology via streamflow alone was sufficient to switch the population's fixed point to $M^*=0$. If, on the other hand, sediment generation did change along with hydrology (black triangle for BLUC, red circle for ALUC), the respective α, β are farther from the regime transition line in both BLUC and ALUC periods, indicating an even more drastic change in the rate at which the populations approach steady state. In either case of altered hydrology, altered sediment production or both, a population growing toward its effective carrying capacity in BLUC conditions declines toward extirpation under ALUC conditions.

5. Concluding Remarks and Perspective: Sustainability Through Vulnerability Science

Environmental systems undergoing change often result in unexpected regime shifts rather than gradual responses to change (e.g., see schematic in Figure 13). For the MRB system, hydrology is the main driver of change and ecological vulnerability rests on sediment amplification that puts chronic stress on mussel populations. As discussed in this paper, an approach for framing an integrated study of the sustainability of agricultural landscapes might evolve around the following questions: (1) What is the interplay of climate and human-induced changes on the hydrology of the watershed? (2) What is the cascade of changes from hydrology to sediment production and transport, to stream geomorphologic change, and stream biotic life? (3) In the absence of detailed physical models (challenged with complex physics and a large number of parameters to be calibrated), what simpler conceptual models can capture the essential elements of change and help identify hydrologic-ecologic regime shifts?

Our study addressed the above questions in a systematic and quantitative way. We documented the nature of hydrologic change at the daily hydrograph and streamflow dynamics and showed via a simplified ecological model how the altered hydrology is bound to lead to extirpation of the native mussel population for

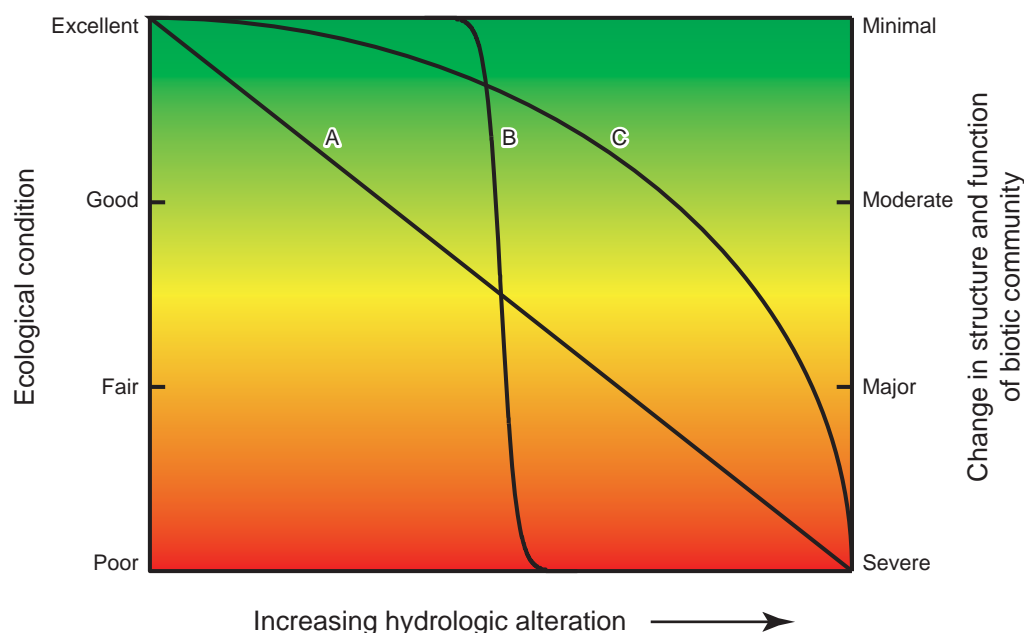


Figure 13. Conceptual flow-ecology curves showing how hydrologic alterations might impact ecological conditions in a river or watershed: (a) linear, (b) threshold or abrupt regime shift, and (c) curvilinear. Reproduced from Blann and Kendy [2012] after Davies and Jackson [2006].

the basin of study. Using the methodologies presented herein, the trade-offs between altering the hydrology and/or the water-sediment production regime of the watershed to avoid transitioning from a healthy population to extirpation in native mussel population can be further studied, thus providing useful guidance for management of the basin. Specifically, a change in either hydrology (e.g., via strategically positioned water retention structures) and/or reduced sediment production (e.g., via riparian vegetation or other stabilization methods) would be needed to avoid ecological collapse, and the costs and benefits can be evaluated for the particular system at hand. By setting desirable targets of sediment reduction and having a detailed knowledge of the sediment-producing geomorphic features, such as ravines, bluffs channel banks relative to the river network (e.g., from a high-resolution LiDAR topographic map, see *Pasalacqua et al.* [2012]), the exact locations where management would provide the highest returns could be identified.

We argue here that in our often-limited capacity to accurately predict the future, decisions toward sustainability could be informed by focusing on the most essential drivers of change, understanding system functionality, and quantifying how the envelope of change would project to the envelope of response. We call this framework “sustainability through vulnerability science.” Indeed, as demonstrated in this paper, it is possible to interrogate complex systems in such a way that useful insight on the long-term cascade of changes can be gained by using a systems perspective and focusing on the variables that would exert the most significant change. A similar framework of analysis as the one discussed in this paper was adopted for identifying emergent hot spots of geomorphic change in the MRB as dictated by river topology and sediment dynamics [Czuba and Foufoula-Georgiou, 2015] and for studying sustainability of deltaic systems via identifying where changes would most drastically affect water and sediment delivery to the shoreline [Tejedor et al., 2015a, 2015b].

On the opportunity of the fiftieth anniversary of Water Resources Research (WRR), it is appropriate to note that WRR has been a pioneer in taking a systems approach to studying hydrologic systems at the intersection of geomorphology, ecology, meteorology, and socioeconomics and in promoting the use of advanced analytical methodologies for practical problems (e.g., WRR 1966 special issue on *Analytical Methods in Hydrology* and WRR 1972 special issue on *Water Resources Systems*). It is hard to imagine what the next 50 years of WRR will bring, but certainly it will continue to lead disciplinary and interdisciplinary hydrologic sciences and engineering, setting new paradigms of approaching increasingly complex and challenging problems while providing science-based solutions.

Appendix A: Continuous Wavelet Transform

The continuous wavelet transform (CWT) of a series $x(t)$ provides a time-frequency decomposition where at location b and scale a , the energy of the signal is captured by the square of the wavelet coefficient $T(a, b)$ given by

$$T(a, b) = \frac{1}{\sqrt{a}} \int_{-\infty}^{\infty} x(t) \psi^* \left(\frac{t-b}{a} \right) dt \quad (A1)$$

where $\psi(t)$ is the mother wavelet and $\psi^*(t)$ denotes its complex conjugate. Here we used the Morlet wavelet, a complex wavelet given as:

$$\psi(t) = \frac{1}{\pi^{1/4}} \left(e^{j2\pi f_0 t} - e^{-(2\pi f_0)^2/2} \right) e^{-t^2/2} \quad (A2)$$

The $\pi^{-1/4}$ term ensures that the wavelet has unit energy and the second term in the brackets (correction term) corrects for the nonzero mean of the complex sinusoid of the first term. In practice, this correction term becomes negligible for values of $f_0 \gg 0$ simplifying the above equation to

$$\psi(t) = \frac{1}{\pi^{1/4}} e^{j2\pi f_0 t} e^{-t^2/2} \quad (A3)$$

This form reveals that the Morlet wavelet is simply a complex wave contained within a Gaussian envelope (centered at zero and of unit standard deviation for the mother wavelet). The Fourier transform of this wavelet is a Gaussian function centered at f_0 which serves as the characteristic frequency of the mother

wavelet and determines the number of effective (nonzero amplitude) sinusoidal waveforms contained within the Gaussian envelope. Larger f_0 (and hence the larger the number of cycles within the Gaussian envelope) corresponds to better frequency localization at the expense of time localization. In practice, a value of $f_0=0.849$ ($=\sqrt{1/(2 \ln 2)}$) is used making the simplified equation (A3) applicable and enclosing three effective sinusoidal waveforms within the Gaussian envelope with the amplitude of the central peak twice as large as the amplitudes of the two smaller adjacent peaks [see Daubechies, 1992; Kumar and Foufoula-Georgiou, 1997; Torrence and Compo, 1998]. This choice of central pass frequency ensures a good frequency localization without compromising the time localization. The mother wavelet $\psi(t)$ (scale $a = 1$) captures the energy corresponding to frequency $f_0=0.849$ (the central frequency of the Gaussian spectrum of $\psi(t)$). By scaling the mother wavelet (dilated $a > 1$ or contracted $a < 1$), the energy at lower and higher frequencies, $f_{0/a}$, is captured. This provides the conversion of frequency to scale used in the plots of Figure 7. The Morlet wavelet is a commonly used wavelet for CWT analysis, sometimes preferable to the Mexican hat wavelet since it allows a phase analysis (not used here) and has minimum Heisenberg uncertainty achieving optimal compromise between time and frequency localization [e.g., Addison, 2002].

Appendix B: Phase Space Embedding and Attractor Reconstruction

The theory of nonlinear dynamics exploits the underlying dynamic structure of a system of coupled and independent evolving variables by reconstructing its attractor in a phase space. Although it has roots in deterministic, noise-free nonlinear systems, its utility for the analysis of observed data has been proven in many fields of study (see Schreiber [1999] for a thorough and accessible review).

Phase space refers to a space in which all possible states of a system are represented. For example, a phase space for the Lorenz system of equations ($\dot{x}=-\sigma(x-y)$; $\dot{y}=-x(\rho-z)$; $\dot{z}=xy-\beta z$), where a dot indicates a time derivative, with given parameters σ , ρ , and β [Sparrow, 1982] can be constructed by assigning each independent variable an axis in space. Within this space, any $(x(t), y(t), z(t))$ triplet completely specifies the state of the system at time t . Integrating the Lorenz equations forward in time and plotting them in the phase space reveals a trajectory of the dynamic system. Given sufficient integration time, the trajectory will delineate the boundary of the underlying attractor. An attractor may be thought of as the geometric structure in phase-space toward which trajectories tend to evolve regardless of the system's initial condition. Phase space embeddings can reveal otherwise hidden structure in time series measurements from dynamical systems. However, unlike constructed models such as the Lorenz attractor, evolution equations are rarely known in natural systems, preventing direct reconstruction of an attractor. The acclaimed embedding theorem of Takens [1981] provided a way to reconstruct attractors from only a single scalar measurement of the dynamical system, provided that the scalar measurement couples all the degrees of freedom of the system:

$$\vec{s}_n = (s_{n-(m-0)\tau}, s_{n-(m-1)\tau}, \dots, s_n) \quad (B1)$$

where \vec{s}_n is a time delayed vector formed from the original data series s_n , n is the number of data points in s_n , m is the embedding dimension, and τ is the delay parameter. Each vector \vec{s}_n serves as an independent axis of the phase space. The literature contains extensive guidance for selecting embedding parameters, but optimal selection is application dependent [Kantz and Schreiber, 2004]. Embedding dimension and delay parameters were selected here such that the attractor "unfolds" without destroying its structure. False nearest neighbors and mutual information [Abarbanel, 1996] analyses guided our selection of m and τ , respectively.

Time delay embedding theorems for attractor reconstruction [Takens, 1981; Sauer et al., 1991] rest upon assumptions that are seldom fulfilled in natural systems. Most notably, a proper reconstruction requires infinite, noise-free trajectories. However, these requirements have not prevented applications of the theories to a host of problems including environmental, financial, physiological, and others (see Schreiber [1999] for a thorough, accessible review and discussion of the potential pitfalls of applying the theory to real data). If proper care is taken, phase space reconstruction captures deterministic nonlinearity even in the presence of noise.

The analyses herein used the following embedding parameters: daily streamflow (Q): $m = 3$, $\tau = 20$ days and daily precipitation (P): $m = 4$, $\tau = 10$ days.

Appendix C: Transportation Distance Metric for Phase Space Comparison

Transportation distance is computed as follows: two time series G and H are embedded into an m dimensional space \mathbf{R}^m via time delay embedding. The domain occupied by their attractors is discretized into B boxes by dividing each m_i axis into $B^{1/m}$ segments. The probability that attractor G occupies box B_i is estimated as $g_i(B_i) = N(G, B_i)/N(G)$, where $N(G, B_i)$ is the number of points in series G that lie within box B_i and $N(G)$ is the length of series G. The discretization of \mathbf{R}^m into boxes may be performed such that either (a) each box is the same size (equally spaced bins), or (b) each box contains the same probability (equal probability bins). We employ the latter method herein as it adds robustness against outliers. Now, let $\mu_{ij} > 0$ represent the amount of "mass" shipped from box B_i to B_j according to transportation plan μ . To preserve initial and final distributions of G and H, we require that

$$\begin{aligned}\sum_{j=1}^N \mu_{ij} &= g_i, & i &= 1, \dots, N \text{ and} \\ \sum_{i=1}^N \mu_{ij} &= h_j, & j &= 1, \dots, N\end{aligned}\quad (C1)$$

Finally, let $M(g, h)$ represent all transportation plans meeting these requirements, and then the transportation distance may be defined as the minimized transportation cost

$$d_T(g, h) = \inf_{\mu \in M(g, h)} \sum_{i,j=1}^N \mu_{ij} \delta_{ij} \quad (C2)$$

where δ_{ij} is a taxi cab metric normalized to the embedding dimension between the centers of B_i and B_j . Thus, the transportation distance in effect measures the least amount of work required to ensure equal probability of both attractors across all B boxes.

The analyses herein used the following discretization parameters for d_T : daily streamflow (Q): $m = 3$, $B^{1/m} = 10$ and daily precipitation (P): $m = 4$, $B^{1/m} = 5$.

Appendix D: Coupled Hydrology-Ecology Dynamic Process Interaction Model

The evolution equations (D1)–(D3) of the process-based interaction mussel population density model are given in terms of parameterized functionals $f_i(\cdot)$. Note that $r_t = f_5(S_t)$ and $\eta_t = f_6(C_t)$ as discussed in this work in section 4.1. That is, the growth rate parameter is a function of the suspended sediment concentration and the mussel carrying capacity modifier depends on the logically modeled phytoplankton population density as chlorophyll-a concentration. For explicit expressions of the functional relationships, parameter values, and insight into their interactions, refer to Hansen et al. [2015]. Model parameters for this work were assigned exactly as Site 6—Redwood—R. Falls [Hansen et al., 2015, Table 2].

$$\frac{dS_t}{dt} = \underbrace{f_1(Q_t)}_{\text{flow dependent suspended sediment generation rate}} - \underbrace{f_2(M_t, S_t, Q_t)}_{\text{mussel filtration rate}} S_t \quad (D1)$$

$$\frac{dC_t}{dt} = \underbrace{f_3(S_t)}_{\text{sediment modulated phytoplankton growth rate}} \underbrace{C_t \left(1 - \frac{C_t}{K_C}\right)}_{\text{logistic growth of phytoplankton pop. with carrying capacity } K_C} - \left(\underbrace{f_4(Q_t)}_{\text{streamflow dilution of phytoplankton}} + \underbrace{f_2(M_t, S_t, Q_t)}_{\text{mussel filtration rate}} \right) C_t \quad (D2)$$

$$\frac{dM_t}{dt} = \underbrace{f_5(S_t)}_{\substack{\text{sediment} \\ \text{modulated} \\ \text{mussel} \\ \text{pop. growth} \\ \text{rate}}} \underbrace{M_t \left(1 - \frac{M_t}{f_6(C_t)} \right)}_{\substack{\text{logistic growth of} \\ \text{mussel pop. with food} \\ \text{modified effective} \\ \text{carrying capacity}}} \quad (\text{D3})$$

Appendix E: Constructing and Understanding Stability Landscapes

The potential (or stability landscape) V_t is defined such that the slope of the potential gives the rate of change of the system variable of interest [Strogatz, 2000]. Specifically,

$$\frac{dV_t}{dM} \equiv -\dot{M}_t \quad (\text{E1})$$

where the negative sign enforces the convention of positive \dot{M}_t when moving from high to low in the positive M direction on the stability landscape or potential V_t . The potential or stability landscape is thus obtained analytically by integrating equation (E1) with respect to M as

$$V_t = - \int \dot{M}_t dM \quad (\text{E2})$$

Upon substituting equation (2) into equation (E2) and integrating, the equation for the potential is given by

$$V_t = r_t M_t^2 \left(\frac{1}{3\eta_t K_M} M_t - \frac{1}{2} \right) + C \quad (\text{E3})$$

where C is a constant of integration set equal to zero.

A more intuitive way to think about the dynamics of equation (2) is to consider its stability landscape or potential (both terms are used interchangeably herein) shown in Figure 11b. Imagine placing an inertia-less ball somewhere along one of the potential curves and letting it roll toward equilibrium. Wherever it comes to rest (at a minimum) is a stable fixed point, because the ball will return to this point following a perturbation. The steepness of the slope indicates how quickly a steady state is attained. If the ball is precisely on top of a hill, the system is at an unstable fixed point as a slight perturbation will send it rolling down the hill.

Acknowledgments

This research was funded by NSF grant EAR-1209402 under the Water Sustainability and Climate Program (WSC): REACH (REsilience under Accelerated CHange) and benefited from collaborations made possible by NSF grants EAR-1242458 (LIFE: Linked Institutions for Future Earth) and EAR-1342944 (Delta Sustainability). The first author also acknowledges support provided by the Joseph T. and Rose S. Ling endowed chair. In Figure 1, the wheat image was courtesy of Daniel X. O’Neil and the soybean image was courtesy of the United Soybean Board; other images were courtesy of Patrick Belmont. All data analyzed in this paper were obtained from the USGS, NOAA, or USDA and are available from their respective websites. We thank Alberto Montanari and two anonymous reviewers for useful comments.

References

- Abarbanel, H. D. I. (1996), *Analysis of Observed Chaotic Data*, Springer, N. Y.
- Addison, P. S. (2002), *The Illustrated Wavelet Transform Handbook—Introductory Theory and Applications in Science, Engineering, Medicine and Finance*, 353 pp., Inst. of Phys. Publ., Philadelphia, Pa.
- Angel, J. R., and F. A. Huff (1997), Changes in heavy rainfall in the Midwestern United States, *J. Water Resour. Plann. Manage.*, 123(4), 246–249, doi:10.1061/(ASCE)0733-9496(1997)123:4(246).
- Belmont, P. (2011), Floodplain width adjustments in response to rapid base level fall and knickpoint migration, *Geomorphology*, 128, 92–102, doi:10.1016/j.geomorph.2010.12.026.
- Belmont, P., et al. (2011), Large shift in source of fine sediment in the Upper Mississippi River, *Environ. Sci. Technol.*, 45, 8804–8810, doi:10.1021/es2019109.
- Biswal, B., and M. Marani (2010), Geomorphological origin of recession curves, *Geophys. Res. Lett.*, 37, L24403, doi:10.1029/2010GL045415.
- Blann, K., and E. Kendy (2012), *Developing Ecological Criteria for Sustainable Water Management in Minnesota*, 129 pp., The Nat. Conservancy, Cushing, Minn.
- Blann, K. L., J. L. Anderson, G. R. Sands, and B. Vondracek (2009), Effects of agricultural drainage on aquatic ecosystems: A review, *Crit. Rev. Environ. Sci. Technol.*, 39(11), 909–1001, doi:10.1080/10643380801977966.
- Brutsaert, W., and J. L. Nieber (1977), Regionalized drought flow hydrographs from a mature glaciated plateau, *Water Resour. Res.*, 13(3), 637–643, doi:10.1029/WR013i003p00637.
- Carlisle, D. M., D. M. Wolock, and M. R. Meador (2011), Alteration of streamflow magnitudes and potential ecological consequences: A multi-regional assessment, *Frontiers Ecol. Environ.*, 9(5), 264–270, doi:10.1890/100053.
- Changnon, S. A., and K. E. Kunkel (1995), Climate-related fluctuations in Midwestern floods during 1921–1985, *J. Water Resour. Plann. Manage.*, 121(4), 326–334, doi:10.1061/(ASCE)0733-9496(1995)121:4(326).
- Chen, B., and W. F. Krajewski (2015), Recession analysis across scales: The impact of both random and nonrandom spatial variability on aggregated hydrologic response, *J. Hydrol.*, 523, 97–106, doi:10.1016/j.jhydrol.2015.01.049.
- Czuba, J. A., and E. Foufoula-Georgiou (2015), Dynamic connectivity in a fluvial network for identifying hotspots of geomorphic change, *Water Resour. Res.*, 51(3), 1401–1421, doi:10.1002/2014WR016139.
- Dadaser-Celik, F., and H. G. Stefan (2009), Stream flow response to climate in Minnesota, *Proj. Rep.* 510, 118 pp., St. Anthony Falls Lab., Univ. of Minn., Minneapolis.

- Dahl, T. E., and G. J. Allord (1996), History of wetlands in the conterminous United States, in *National Water Summary on Wetland Resources, U.S. Geol. Surv. Water Supply Pap.*, 2425, U.S. Geol. Surv., Reston, Va. [Available at <http://water.usgs.gov/nwsum/WSP2425/history.html>.]
- Daubechies, I. (1992), *Ten Lectures on Wavelets*, 350 pp., Soc. for Ind. and Appl. Math., Philadelphia, Pa., doi:10.1137/1.9781611970104.
- Davies, S. P., and S. K. Jackson (2006), The biological condition gradient: A descriptive model for interpreting change in aquatic ecosystems, *Ecol. Appl.*, 16(4), 1251–1266, doi:10.1890/1051-0761(2006)016[1251:TBCGAD]2.0.CO;2.
- De Schepper, G., R. Therrien, J. C. Refsgaard, and A. L. Hansen (2015), Simulating coupled surface and subsurface water flow in a tile-drained agricultural catchment, *J. Hydrol.*, 521, 374–388, doi:10.1016/j.jhydrol.2014.12.035.
- Douglas, E. M., R. M. Vogel, and C. N. Kroll (2000), Trends in floods and low flows in the United States: Impact of spatial correlation, *J. Hydrol.*, 240(1–2), 90–105, doi:10.1016/S0022-1694(00)00336-X.
- Dupuis, D. J. (2007), Using Copulas in hydrology: Benefits, cautions, and issues, *J. Hydrol. Eng.*, 12(4), 381–393, doi:10.1061/(ASCE)1084-0699(2007)12:4(381).
- Engstrom, D. R., J. E. Almendinger, and J. A. Wolin (2009), Historical changes in sediment and phosphorus loading to the upper Mississippi River: Mass-balance reconstructions from the sediments of Lake Pepin, *J. Paleolimnol.*, 41(4), 563–588, doi:10.1007/s10933-008-9292-5.
- Favre, A.-C., S. El Adlouni, L. Perreault, N. Thiébaut, and B. Bobée (2004), Multivariate hydrological frequency analysis using copulas, *Water Resour. Res.*, 40, W01101, doi:10.1029/2003WR002456.
- Frans, C., E. Istanbulluoglu, V. Mishra, F. Munoz-Arriola, and D. P. Lettenmaier (2013), Are climatic or land cover changes the dominant cause of runoff trends in the Upper Mississippi River Basin?, *Geophys. Res. Lett.*, 40, 1104–1110, doi:10.1002/grl.50262.
- Gran, K. B., P. Belmont, S. S. Day, N. Finnegan, C. Jennings, J. W. Lauer, and P. R. Wilcock (2011), Landscape evolution in south-central Minnesota and the role of geomorphic history on modern erosional processes, *GSA Today*, 21(9), 7–9, doi:10.1130/G121A.1.
- Gran, K. B., N. Finnegan, A. L. Johnson, P. Belmont, C. Wittkop, and T. Rittenour (2013), Landscape evolution, valley excavation, and terrace development following abrupt postglacial base-level fall, *GSA Bull.*, 125(11–12), 1851–1864, doi:10.1130/B30772.1.
- Groisman, P. Y., R. W. Knight, T. R. Karl, D. R. Easterling, B. Sun, and J. H. Lawrimore (2004), Contemporary changes of the hydrological cycle over the contiguous United States: Trends derived from in situ observations, *J. Hydrometeorol.*, 5(1), 64–85, doi:10.1175/1525-7541(2004)005<0064:CCOTH>2.0.CO;2.
- Groisman, P. Y., R. W. Knight, and T. R. Karl (2012), Changes in intense precipitation over the central United States, *J. Hydrometeorol.*, 13(1), 47–66, doi:10.1175/JHM-D-11-039.1.
- Hansen, A. T., J. A. Czuba, J. Schwenk, A. Longjas, M. Danesh-Yazdi, D. J. Hornbach, and E. Foufoula-Georgiou (2015), Coupling freshwater mussel ecology and river dynamics using a simplified dynamic interaction model, *Freshwater Science*.
- Harman, C. J., M. Sivapalan, and P. Kumar (2009), Power law catchment-scale recessions arising from heterogeneous linear small-scale dynamics, *Water Resour. Res.*, 45, W09404, doi:10.1029/2008WR007392.
- Higgins, R. W., and V. E. Kousky (2013), Changes in observed daily precipitation over the United States between 1950–79 and 1980–2009, *J. Hydrometeorol.*, 14(1), 105–121, doi:10.1175/JHM-D-12-062.1.
- Hirsch, R. M., and K. R. Ryberg (2012), Has the magnitude of floods across the USA changed with global CO₂ levels?, *Hydrol. Sci. J.*, 57(1), 1–9, doi:10.1080/02626667.2011.621895.
- Joiner, J., et al. (2014), The seasonal cycle of satellite chlorophyll fluorescence observations and its relationship to vegetation phenology and ecosystem atmosphere carbon exchange, *Remote Sens. Environ.*, 152, 375–391, doi:10.1016/j.rse.2014.06.022.
- Kantorovich, L. (1958), On the translocation of masses, *Manage. Sci.*, 5(1), 1–4, doi:10.1287/mnsc.5.1.1.
- Kantz, H., and T. Schreiber (2004), *Nonlinear Time Series Analysis*, vol. 7, Cambridge Univ. Press, Cambridge, U. K.
- Karl, T. R., R. W. Knight, D. R. Easterling, and R. G. Quayle (1996), Indices of climate change for the United States, *Bull. Am. Meteorol. Soc.*, 77(2), 279–292, doi:10.1175/1520-0477(1996)077<0279:IOCCFT>2.0.CO;2.
- Kelley, D. W., and E. A. Nater (2000), Historical sediment flux from three watersheds into Lake Pepin, Minnesota, USA, *J. Environ. Qual.*, 29, 561–568, doi:10.2134/jeq2000.00472425002900020025x.
- Keylock, C. J. (2008), Improved preservation of autocorrelative structure in surrogate data using an initial wavelet step, *Nonlinear Processes Geophys.*, 15, 435–444, doi:10.5194/npg-15–435-2008.
- Keylock, C. J. (2010), Characterizing the structure of nonlinear systems using gradual wavelet reconstruction, *Nonlinear Processes Geophys.*, 17, 615–632, doi:10.5194/npg-17–615-2010.
- Kirchner, J. W. (2009), Catchments as simple dynamical systems: Catchment characterization, rainfall-runoff modeling, and doing hydrology backward, *Water Resour. Res.*, 45, W02429, doi:10.1029/2008WR006912.
- Kirsch, N. A., S. A. Hanson, P. A. Renard, and J. W. Enblom (1985), *Biological Survey of the Minnesota River, Spec. Publ.* 139, 85 pp., Minn. Dep. of Nat. Resour. Fish., St. Paul. [Available at http://files.dnr.state.mn.us/publications/fisheries/special_reports/139.pdf.]
- Konar, M., M. J. Todd, R. Muneepeerakul, A. Rinaldo, and I. Rodriguez-Iturbe (2013), Hydrology as a driver of biodiversity: Controls on carrying capacity, niche formation, and dispersal, *Adv. Water Resour.*, 51, 317–325, doi:10.1016/j.advwatres.2012.02.009.
- Kumar, P., and E. Foufoula-Georgiou (1997), Wavelet analysis for geophysical applications, *Rev. Geophys.*, 35(4), 385–412, doi:10.1029/97RG00427.
- Legislative Coordinating Commission (2014), *Minnesota's Legacy: Watch the Progress*, The Minn. State Legislature, St. Paul. [Available at <http://www.legis.leg.mn/>.]
- Lettenmaier, D. P., E. F. Wood, and J. R. Wallis (1994), Hydro-climatological trends in the continental United States, 1948–88, *J. Clim.*, 7(4), 586–607, doi:10.1175/1520-0442(1994)007<0586:HCTIC>2.0.CO;2.
- Lins, H. F., and J. R. Slack (1999), Streamflow trends in the United States, *Geophys. Res. Lett.*, 26(2), 227–230, doi:10.1029/1998GL900291.
- Marschner, F. J. (1974), The original vegetation of Minnesota, a map compiled in 1930 by F.J. Marschner under the direction of M.L. Heinselman of the United States Forest Service, scale 1:500,000, Cartogr. Lab. of the Dep. of Geogr., Univ. of Minn., St. Paul.
- Michaels, P. J., P. C. Knappenberger, O. W. Frauenfeld, and R. E. Davis (2004), Trends in precipitation on the wettest days of the year across the contiguous USA, *Int. J. Climatol.*, 24(15), 1873–1882, doi:10.1002/joc.1102.
- Milly, P. C. D., and K. A. Dunne (2001), Trends in evaporation and surface cooling in the Mississippi River Basin, *Geophys. Res. Lett.*, 28(7), 1219–1222, doi:10.1029/2000GL012321.
- Moeckel, R., and B. Murray (1997), Measuring the distance between time series, *Physica D*, 102(3), 187–194, doi:10.1016/S0167-2789(96)00154-6.
- Moline, R. T. (1969), The modification of the wet prairie in southern Minnesota, *PhD thesis*, 283 pp., Univ. of Minn., Minneapolis.
- Musser, K., S. Kudelka, and R. Moore (2009), Minnesota River Basin trends, water resources center report, 64 pp., Minn. State Univ., Mankato. [Available at <http://mrbdc.mnsu.edu/minnesota-river-basin-trends-report>.]

- National Oceanic and Atmospheric Administration (2015), National Climatic Data Center, Climate Data Online, <http://www.ncdc.noaa.gov/cdo-web/>, Natl. Clim. Data Cent., Asheville, N. C.
- Nelsen, R. B. (1999), *An Introduction to Copulas, Lecture Notes in Statistics*, vol. 139, 221 pp., Springer, N. Y.
- Novotny, E. V., and H. G. Stefan (2007), Stream flow in Minnesota: Indicator of climate change, *J. Hydrol.*, 334(3–4), 319–333, doi:10.1016/j.jhydrol.2006.10.011.
- Ojakangas, R. W., and C. L. Matsch (1982), *Minnesota's Geology*, 255 pp., Univ. of Minn. Press, Minneapolis.
- Passalacqua, P., P. Belmont, and E. Foufoula-Georgiou (2012), Automatic geomorphic feature extraction from lidar in flat and engineered landscapes, *Water Resour. Res.*, 48, W03528, doi:10.1029/2011WR010958.
- Pryor, S. C., J. A. Howe, and K. E. Kunkel (2009), How spatially coherent and statistically robust are temporal changes in extreme precipitation in the contiguous USA?, *Int. J. Climatol.*, 29(1), 31–45, doi:10.1002/joc.1696.
- Raymond, P. A., N.-H. Oh, R. E. Turner, and W. Broussard (2008), Anthropogenically enhanced fluxes of water and carbon from the Mississippi River, *Nature*, 451, 449–452, doi:10.1038/nature06505.
- Rüschenhof, L. (2009), On the distributional transform, Sklar's theorem, and the empirical copula process, *J. Stat. Plann. Inference*, 139(11), 3921–3927, doi:10.1016/j.jspi.2009.05.030.
- Salvadori, G., and C. De Michele (2007), On the use of Copulas in hydrology: Theory and practice, *J. Hydrol. Eng.*, 12(4), 369–380, doi:10.1061/(ASCE)1084-0699(2007)12:4(369).
- Sauer, T., J. A. Yorke, and M. Casdagli (1991), Embedology, *J. Stat. Phys.*, 65(3–4), 579–616, doi:10.1007/BF01053745.
- Schilling, K. E., and M. Helmers (2008), Effects of subsurface drainage tiles on streamflow in Iowa agricultural watersheds: Exploratory hydrograph analysis, *Hydrol. Processes*, 22(23), 4497–4506, doi:10.1002/hyp.7052.
- Schilling, K. E., and R. D. Libra (2003), Increased baseflow in Iowa over the second half of the 20th century, *J. Am. Water Resour. Assoc.*, 39(4), 851–860, doi:10.1111/j.1752-1688.2003.tb04410.x.
- Schilling, K. E., K.-S. Chan, H. Liu, and Y.-K. Zhang (2010), Quantifying the effect of land use/land cover change on increasing discharge in the Upper Mississippi River, *J. Hydrol.*, 387(3–4), 343–345, doi:10.1016/j.jhydrol.2010.04.019.
- Schottler, S. P., J. Ulrich, P. Belmont, R. Moore, J. W. Lauer, D. R. Engstrom, and J. E. Almendinger (2014), Twentieth century agricultural drainage creates more erosive rivers, *Hydrol. Processes*, 28(4), 1951–1961, doi:10.1002/hyp.9738.
- Schreiber, T. (1999), Interdisciplinary application of nonlinear time series methods, *Phys. Rep.*, 308(1), 1–64, doi:10.1016/S0370-1573(98)00035-0.
- Shaw, S. B., and S. J. Riha (2012), Examining individual recession events instead of a data cloud: Using a modified interpretation of dQ/dt-Q streamflow recession in glaciated watersheds to better inform models of low flow, *J. Hydrol.*, 434–435, 46–54, doi:10.1016/j.jhydrol.2012.02.034.
- Sparrow, C. (1982), *The Lorenz Equations: Bifurcations, Chaos, and Strange Attractors*, vol. 41, Springer, N. Y.
- Strogatz, S. H. (2000), *Nonlinear Dynamics and Chaos: With Applications to Physics, Biology, Chemistry, and Engineering, Studies in Nonlinearity*, 512 pp., Westview Press, Cambridge, Mass.
- Stuyt, L. C. P. M., W. Dierikx, and J. Martínez Beltrán (2005), Materials for subsurface land drainage systems, *FAO Irrig. Drain. Pap.* 60, rev. 1, 183 pp., Food and Agric. Organ. of the U. N., Rome.
- Takens, F. (1981), *Detecting Strange Attractors in Turbulence*, Springer, Berlin.
- Tejedor, A., A. Longjas, I. Zaliapin, and E. Foufoula-Georgiou (2015a), Delta channel networks: 1. A graph-theoretic approach for studying connectivity and steady state transport on deltaic surfaces, *Water Resour. Res.*, doi:10.1002/2014WR016577, in press.
- Tejedor, A., A. Longjas, I. Zaliapin, and E. Foufoula-Georgiou (2015b), Delta Channel Networks: 2. Metrics of topologic and dynamic complexity for delta comparison, physical inference, and vulnerability assessment, *Water Resour. Res.*, doi:10.1002/2014WR016604, in press.
- Torrence, C., and G. P. Compo (1998), A practical guide to wavelet analysis, *Bull. Am. Meteorol. Soc.*, 79(1), 61–78, doi:10.1175/1520-0477(1998)079<0061:APGTWA>2.0.CO;2.
- U.S. Department of Agriculture (2015), National Agricultural Statistics Service, CropScape—Cropland data layer, Washington, D. C. [Available at <http://nassgeodata.gmu.edu/CropScape/>.]
- U.S. Department of Agriculture (USDA) (2014), National Agricultural Statistics Service, Data and Statistics, Quick Stats 2.0, Washington, D. C. [Available at <http://quickstats.nass.usda.gov/>.]
- U.S. Geological Survey (2014), USGS Water Data for Minnesota, Reston, Va. [Available at <http://waterdata.usgs.gov/mn/nwis?>.]
- Villarini, G., J. A. Smith, M. L. Baek, R. Vitolo, D. B. Stephenson, and W. F. Krajewski (2011), On the frequency of heavy rainfall for the Midwest of the United States, *J. Hydrol.*, 400(1–2), 103–120, doi:10.1016/j.jhydrol.2011.01.027.
- Walsh, J., et al. (2014), Our changing climate, in *Climate Change Impacts in the United States: The Third National Climate Assessment*, edited by J. M. Melillo, T. C. Richmond, and G. W. Yohe, chap. 2, pp. 19–67, U.S. Global Change Res. Program, Washington, D. C., doi:10.7930/J0KW5CXT.
- Zhang, Y.-K., and K. E. Schilling (2006), Increasing streamflow and baseflow in Mississippi River since the 1940s: Effect of land use change, *J. Hydrol.*, 324(1–4), 412–422, doi:10.1016/j.jhydrol.2005.09.033.